Resting state connectivity alterations in multiple sclerosis revealed by 7 T MRI

Shangming (Forest) Liu

Biomedical Engineering Department

Montreal Neurological Institute

McGill University, Montreal, Quebec

Supervised by Dr. David Rudko

August 2020

A thesis submitted to McGill University in partial fulfillment of the requirements of the degree of Master of Engineering.

Abstract

Multiple Sclerosis (MS) is an autoimmune disease that affects the central nervous system and is characterized by demyelination, axonal loss, and neurodegeneration. Functional connectivity (FC), the temporal correlation of multiple distinct brain regions, characterizes resting state networks (RSN) and may contain useful indicators of MS pathology that are not captured with traditional structural MRI metrics.

In this project, we aimed to elucidate FC differences between a cohort of age/sex matched healthy controls (HC) (n=15), early stage relapsing-remitting MS (RRMS) (n=14) and late stage secondary progressive MS (SPMS) (n=11) patients. Subjects were scanned using high field 7 T MRI to acquire high quality resting state functional MRI data, as well as high resolution anatomical images. RSN's were measured using two methods: (1) group independent component analysis, a fully data-driven technique that uncovered group-specific RSNs, and (2) a correlation matrix approach, implemented by selecting 100 predefined regions of interest (ROIs) across a set of template RSN's. Group differences in FC were measured with reference to MS disability, neuropsychological testing scores, and cortical gray matter thickness.

The RRMS phenotype exhibited globally increased FC compared to HC and SPMS. This was particularly evident within and between the default mode network and executive control network. RRMS subjects also showed statistically significant increases in connectivity within the visual and sensorimotor networks compared to HC in dual regression functional MRI data analysis. A regional connectivity analysis using predefined ROIs revealed increased FC in short-range, posterior DMN regions and disrupted long-range FC in thalamic DMN regions of RRMS subjects compared to HC. The strength of thalamic connections in the DMN was also directly correlated with cognitive processing speed in all three cohorts. Overall, the results of our study suggest possible short-term compensatory adaptations in RRMS that may preserve and even strengthen FC in the brain.

Résumé

La sclérose en plaques (SP) est une maladie auto-immune qui affecte le système nerveux central et se caractérise par la démyélinisation, la perte axonale et la neurodégénérescence. La connectivité fonctionnelle (CF), qui est la corrélation temporelle de plusieurs régions cérébrales distinctes, caractérise les réseaux d'état de repos (RSN) et peut contenir des indicateurs utiles de la pathologie de la sclérose en plaques qui ne sont pas capturés avec les mesures IRM structurelles traditionnelles.

Dans le cadre de ce projet, nous avons cherché à élucider les différences de CF entre une cohorte de témoins sains (TS) appariés selon l'âge/le sexe (n=15), les patients atteints de SP récidivante-rémissive au stade précoce (RRPS) (n=14) et les patients atteints de SP progressive au stade secondaire tardif (SPPS) (n=11). Les sujets ont été scannés à l'aide de l'IRM à champ élevé 7 T pour acquérir des données IRM fonctionnelles de haute qualité à l'état de repos et des images anatomiques à haute résolution. Les RSN ont été mesurés à l'aide de deux méthodes : (1) l'analyse des composantes indépendantes du groupe, qui est une technique entièrement axée sur les données qui a permis de découvrir les RSN propres au groupe, et (2) une approche matricielle de corrélation, mise en œuvre en sélectionnant 100 régions d'intérêt (ROI) prédéfinies dans un ensemble de RSN modèles. Les différences entre les groupes ont été mesurées en fonction de l'incapacité liée à la sclérose en plaques, des résultats des tests neuropsychologiques et de l'épaisseur de la matière grise corticale.

Le phénotype RRPS présentait une augmentation globale de la CF par rapport au phénotype TS et au phénotype SPPS. Cela était particulièrement évident à l'intérieur et entre le réseau de mode par défaut (RMD) et le réseau de contrôle exécutif (RCE). Les sujets atteints de RRPS ont également montré des augmentations statistiquement significatives de la connectivité au sein du réseau visual et sensorimoteur comparativement aux TS dans

l’analyse des données IRM fonctionnelles de double régression. Une méthode d'analyse de la connectivité régionale utilisant des ROI prédéfinis a révélé une augmentation de CF à courte portée dans les régions RMD postérieures et les connexions RMD thalamiques à longue portée ont été pertubées dans RRPS par rapport à TS. Les connexions thalamiques dans le RMD étaient également directement corrélées à la vitesse de traitement cognitif dans les trois cohortes. Dans l’ensemble, les résultats de notre étude suggèrent d’éventuelles adaptations compensatoires, à court terme, des patients atteints de RRPS qui pourraient préserver et même renforcer la CF dans le cerveau.

Acknowledgements

This project was supervised by Dr. David Rudko at McGill University. I would like to acknowledge his excellent guidance, mentorship, and support throughout my entire degree program.

I would also like to acknowledge Dr. Bratislav Misic at McGill University for support and sharing his expert knowledge on the Partial Least Squares analysis. Much of the results were made possible with his expertise.

The data collection for this project was a joint effort between researchers at McGill University and the University of Western Ontario. Dr. David Rudko, Dr. Sridar Narayanan, and Dr. Douglas Arnold from McGill University, and Dr. Joseph Gati, Dr. Ravi Menon, and Dr. Sarah Morrow from the University of Western Ontario all contributed to a successful data collection process.

The data was analyzed, and the thesis was written by Shangming (Forest) Liu. Dr. David Rudko provided comments and edited the thesis.

Table of Contents

1. Introduction

The brain, the central organ of the human nervous system, is primarily comprised of white matter, gray matter, and cerebrospinal fluid (CSF). White matter, which composes 60% of soft tissue volume, essentially facilitates the neuronal signal transfer process. Gray matter, the remaining 40% of parenchymal tissue primarily exists as clusters of nuclei in the brain[1]. Gray matter nuclei are often considered the final sites for neuronal signal processing. CSF, a clear and colorless fluid produced by specialized ependymal cells of the brain ventricles, flows throughout the ventricles and spinal cord[1]. CSF serves a myriad of purposes, including nutrient circulation and waste management. It also functions to cushion the brain from external physical forces. The above major components of the brain interact in concert to maintain the homeostatic state of a healthy, functioning brain. They are supported by the blood-brain barrier (BBB), which is a semi-permeable layer mitigating nutrient exchange between the external blood circulation and brain tissue. Disturbances to normal brain homeostasis and BBB integrity may arise from a wide range of conditions, including physical trauma such as concussion, natural cell death due to aging, or neuro-inflammation due to multiple sclerosis (MS).

MS is a neuroinflammatory autoimmune disease in which the myelin sheath surrounding the white matter of the central nervous system is attacked and destroyed by pathogenic CD4+ and CD8+ cells, which are further supported by B-cells and others in the immune system[2] . Currently, both the biological mechanism and the disease course of MS are incompletely understood[3]. However, substantial progress has been made in the last 20 years

addressing the symptoms and slowing disease progression. The primary neuroinflammatory insult in MS involves degradation of white matter (WM) myelin[3]. This adversely affects signal communication, given that WM is overwhelmingly responsible for connecting sensory neurons. Depending on the severity of demyelination and axonal loss in MS, symptoms may first manifest as a decline in physical motor skills (in early stage MS), followed by more severe consequences such as confinement to a wheelchair.

The early diagnosis and treatment of MS has become an increasingly important area of study and disease modifying therapies (DMTs) are most effective in the earliest stages of MS[4]. Attacking the disease as early as possible has generated the greatest success in preserving brain structure, cognitive and motor function, and overall quality of life[5]. When the disease enters the progressive stage, the patient's options for effective DMT's decreases substantially and the neurodegenerative mechanisms become more complex. Constantly improving anti-inflammatory DMT's can slow disease progression and address the autoimmune response but evaluating the efficacy of such therapies in a quantitative manner remains challenging[6]. The introduction of magnetic resonance imaging (MRI) in the 1970's, and its rapid advancement in the decades thereafter, has enabled numerous improvements in neuroimaging-based detection and monitoring of demyelination in MS. Novel imaging techniques have improved the early detection and diagnosis of MS, and results are highly complementary with neurological and biological testing[7].

Current applications of MRI for monitoring MS go far beyond simple anatomical imaging and include diffusion tensor imaging (DTI), susceptibility weighted imaging (SWI), and BOLD fMRI, among others. White matter tract-specific demyelination and structural

integrity can be detected by mapping water diffusion using DTI[7]. In lesions that manifest in gray matter and normal appearing white matter, iron level often increases, which increases magnetic susceptibility[8]. Quantitative susceptibility mapping is a method of SWI that can be used to detect such increased susceptibility and has shown up to 50% increases in lesion detection over conventional MRI[7]. Alterations in neuronal activity and metabolism in gray matter can be indirectly detected via the functional MRI blood-oxygen level dependent (BOLD) signal.

This thesis focuses on the resting state functional MRI (rs-fMRI) signal and, specifically, on network-level rs-fMRI alterations in MS. Brain networks, as derived from rs-fMRI, are synchronous BOLD signal fluctuations. They are detected using MRI examinations performed on a subject "at rest" - not subject to an external stimulus and defined by the synchronous BOLD activity occurring in multiple regions of the brain. One of the first RSN's to be discovered was the default mode network (DMN), which comprises of activation in the orbital frontal cortex, prefrontal cortex, posterior cingulate cortex and parietal lobe.

The precise biological mechanisms underlying synchronous neuronal activation in rs-fMRI are unknown. Although RSN's generally correlate well with white-matter structural networks[9], there are still many examples of synchronous BOLD activity occurring without any direct structural connections[10]. Previous research has observed that rs-fMRI network level changes occur with age[11], neurological disease[12] and traumatic brain injury[13], among others. In this study, our goal is to closely examine the networks of the brain within two MS phenotypes: (1) Relapsing-Remitting MS (RRMS), a form of early onset MS in which patients experience relapses of symptoms followed by remission, and (2) Secondary-Progressive MS

(SPMS), a later stage of the disease in which symptoms get progressively worse. The two MS phenotypes are compared to a healthy, age and education-matched group of controls. Resting state network changes are observed, accounting for such physical parameters as atrophy and cortical thickness, as well as such cognition and other clinical test scores.

2. Background

2.1 Magnetic Resonance Imaging

Fundamental Physics

Magnetic Resonance Imaging (MRI) is based on the principle of nuclear magnetic resonance (NMR). The fundamental physical mechanism that governs NMR is the interaction of a nucleus with an external magnetic field. Hydrogen (^{1}H) is the most abundant MRI-visible nucleus in living tissue. Various tissue structures in the human body, such as muscle and fat differ in hydrogen/proton density. Upon the application of an external magnetic field, B_0, protons align with the direction of the magnetic field and precess. The precession is analogous to gravity acting on a spinning gyroscope. The gyroscope maintains its original spin, but also wobbles (precesses) about the axis of gravitational force.

The precession frequency (omega sign here) of protons in the external magnetic field, B_0, of the MRI magnet is given by the Larmor equation:

$$\omega_0 = \gamma \cdot B_0 \qquad \textbf{(2.1)}$$

Where:

- ω_0 is the precessional, or Larmor frequency, measured in MHz
- γ is the gyromagnetic ratio, a constant equal to 42.57 MHz/Tesla (MHz/T) for hydrogen. Gyromagnetic ratios are a fixed constant for different types of nuclei, and the value is 42.57 MHz/T for protons

- B_0 is the strength of the applied external magnetic field, in T

The net magnetization of a bulk sample of protons in an external magnetic field is denoted by the symbol M_0. The application of a strong external to a sample of results in a small excess of protons in a lower energy state with parallel alignment to the B_0 field. The number of spins in the lower energy state is only a handful of spins per million at typical B_0 field strengths. However, the resulting net magnetization M_0 is large enough to be applied to detect signal in MRI. By applying a radiofrequency (RF) pulse, B_1^+, perpendicular to the B_0 field at the Larmor frequency, precessing protons synchronously rotate or "tip" away from the B_0 axis.

The orientation of final precession is directly dependent on the strength and duration of the applied RF pulse, as determined by the following equation:

$$\alpha = \gamma \cdot B_1 \cdot T_p \qquad \textbf{(2.2)}$$

Where:

- α is the flip angle, which describes extent of rotation or "tipping" away from M_0
- γ is the gyromagnetic ratio in MHz/T
- B_1 is the strength of the applied RF pulse, in T
- T_p is the duration of the pulse, in seconds

Bloch Equations

Subsequent to the application of an externally applied B_1^+ field, protons "relax" back to their equilibrium state. Two different mechanisms govern the dynamics of proton relaxation: (1) spin-lattice relaxation, through which the longitudinal component of

magnetic moment, M_z, returns to the equilibrium state and (2) spin-spin relaxation, in which protons interact with their neighbours through dipolar interactions and the transverse magnetization, M_{xy}, is dephased[14]. Spin-spin relaxation involves energy transfer between neighbouring spins through dipolar and exchange interactions. Spin-lattice relaxation is characterized by the loss of stored energy to the surroundings (lattice).

These two NMR relaxation phenomena were classically modelled by physicist, Felix Bloch, in 1946. Bloch specifically developed a differential equation-based formalism of the longitudinal and transverse relaxation components. The path of vector magnetization over time can be modelled as the cross product of magnetic moment with the static external magnetic field:

$$\frac{\boldsymbol{dM}}{\boldsymbol{dt}} = \boldsymbol{\gamma \cdot M \times B} \qquad \textbf{(2.3)}$$

Where:

- gamma is the gyromagnetic ratio.
- M is the vector magnetic moment.
- B is a generalized expression of the magnetic field.

Equation 2.3 can be expanded into component form as follows:

$$\frac{\boldsymbol{dM}}{\boldsymbol{dt}} = \boldsymbol{\gamma \cdot [(M_y B_z - M_z B_y)\hat{i} + (M_z B_x - M_x B_z)\hat{j} + (M_x B_y - M_y B_x)\hat{k}]} \qquad \textbf{(2.4)}$$

Where B_z is static magnetic field along the Z-axis in the magnet frame of reference and B_x and B_y are magnetic fields rotating in the transverse plane.

In MRI, the transverse rotating external magnetic fields are usually generated by RF coils. The B_x and B_y fields typically vary sinusoidally in the transverse plane:

$$\boldsymbol{B_x = B_1 \cdot \cos(\omega t)} \quad \textbf{(2.5)}$$

$$\boldsymbol{B_y = -B_1 \cdot \sin(\omega t)} \quad \textbf{(2.6)}$$

$$\boldsymbol{B_z = B_0} \quad \textbf{(2.7)}$$

By substituting equations 2.5-2.7 into equation (2.4) and imposing the initial condition of $B_1^+=0$ after completion of a 90 degree RF pulse, with Mx(0)=0, Mz(0)=0, and My(0)=M_0, the Bloch equations can be solved to yield:

$$\boldsymbol{M_x(t) = M_0 \cdot e^{-t/T_2} \cdot \sin(\omega t)} \quad \textbf{(2.8)}$$

$$\boldsymbol{M_y(t) = M_0 \cdot e^{-t/T_2} \cdot \cos(\omega t)} \quad \textbf{(2.9)}$$

$$\boldsymbol{M_z(t) = M_0 \cdot (1 - e^{-t/T_1}) \cdot \cos(\omega t)} \quad \textbf{(2.10)}$$

In equations 2.8-2.10, the T_1 and T_2 constants denote the spin-lattice and spin-spin interactions, respectively. Together, equations 2.8-2.10 model a proton's return to equilibrium and static dephasing after the application of an RF pulse (Cite). The motion of protons returning to equilibrium can be classically understood as an upward spiraling pattern in the shape of a tent[14].

T_1 and T_2 Relaxation

The spin-lattice relaxation time, T_1, is defined as the time required for the longitudinal magnetization (Mz) to return to 63%, of M_0. Similarly, the spin-spin relaxation time (T_2) relaxation time can be classically modeled as an exponential decay based on equations 2.8 and 2.9:

$$\boldsymbol{M_{xy}(t) = M_0 \cdot e^{-t/T_2}} \quad \textbf{(2.11)}$$

The T_2 relaxation time is time required for M_x or M_y to reach 37%, of their initial value before the application of a B_1^+ pulse. Relaxation times are dependent on external magnetic field strength[14]. Some typical values for relaxation times of biological tissue are summarized in table 2.1.

	T1 (ms)		**T2 (ms)**	
	1.5 T	**3 T**	**1.5 T**	**3 T**
Grey Matter	1100	1331	92	80
White Matter	560	832	82	110
Cerebrospinal Fluid	2060	3700	N/A	N/A
Muscle	1075	898	33	29
Fat	200	382	N/A	68

Table 2.1: Typical T_1 and T_2 relaxation time estimates at 1.5 T and 3 T field strengths[15].

In MRI experiments, the measured T_2 is often shorter than that predicted by theory. This difference is partially explained by the presence of local B_0 magnetic field inhomogeneities caused by structures such as iron, myelin, calcium and blood in the human body. When local magnetic field inhomogeneities are present, an additional relaxation component, denoted T_2' (reversible contribution to the transverse relaxation time from local field inhomogeneities) impacts the relaxation behaviour. When local field inhomogeneities are present, transverse relaxation is said to occur via the T_2^* mechanism ("T_2 Star", apparent transverse relaxation time). The T_2^* time is then mathematically denoted as:

$$\boldsymbol{\frac{1}{T_2^*} = \frac{1}{T_2} + \frac{1}{T_2'}} \quad \textbf{(2.12)}$$

Alternatively, equation (2.12) can be written in terms of *relaxation rates*, which are defined as the inverse of the relaxation times:

$$\boldsymbol{R_2^* = R_2 + R_2'} \qquad \textbf{(2.13)}$$

Many types of imaging take advantage of T_2^* contrast. The presence of tissue-local field interactions are particularly relevant for imaging of the blood-oxygen level dependent (BOLD) contrast in fMRI[16].

Controlling Image Contrast Through an MRI Pulse Sequence

In MR imaging, protons are excited through a sequence of timed RF pulses followed by delays. The combination of RF pulses and delays, in conjunction with gradient pulses and signal readout forms an MRI pulse sequence. Two fundamental pulse sequence parameters that critically impact MR image contrast are the echo time, TE, which measures time between RF pulse application and signal acquisition, and the repetition time, TR, which measures time between successive RF pulses. Appropriately varying TE and TR impacts the contrast generated in an MR image. Specifically, selection of TE and TR is usually carried out based on knowledge of T_1 and T_2 relaxation times of tissue[14].

During nuclear relaxation, T_1 and T_2 decay processes occur simultaneously. The T_1 time is longer than T_2 for brain tissue and the signal contribution from T_1 is highest immediately following the RF pulse. For this reason, T_1 weighted imaging uses short TE, with a TR value that aligns with the T_1 values of the target tissue being imaged[15]. T_1-weighted

contrast is very useful for structural MR imaging of the brain, since T_1 values differ appreciably for distinct tissue types in the brain (e.g. white matter, gray matter and cerebrospinal fluid). In T_2-weighted imaging, TR is generally kept long, while the TE is often selected based on the T_2 value of a specific tissue (or group of tissues). T_2-weighted imaging is a standard contrast used to image white matter lesions and tumors in the brain[14].

Magnetic Resonance Imaging System Components

Broadly, MRI systems are comprised of three principal components: the main magnet, the gradient coils, and the radiofrequency coil.

The Magnet

A major component of the MRI system is the main magnet. It is essentially a series of repeating wire loops formed around a hollow cylinder. The majority of clinical and research MRI's utilize superconducting magnets which are cooled to as low as -269 degrees Celsius with liquid helium[15]. Superconducting magnet technology has evolved substantially in the last 20 years. Superconducting metal alloys can now be manufactured to produce strong, consistent static fields for the purposes of MR imaging over large volumes[17]. Specialized human MRI systems, including the high field MRI system employed for imaging in this thesis, can have main magnetic fields in excess of 7 Teslas (T)[17]. Clinical MRI systems generally have magnetic field strengths in the range of 1.5 – 3.0 T.

Gradient Coils

Gradient coils, or simply imaging gradients, are electromagnets used to localize signal through spatial encoding in MRI. Spatial encoding is achieved by creating short term, spatial variations in the B_0 field. This is specifically done by adding or subtracting linear magnetic fields of a given amplitude along the X, Y, and Z axes of the coordinate system of the magnet. The strength of magnetic field gradients used in MRI is typically on the order of 50-80 milli-teslas per meter (mT/m). Two gradient coil performance metrics that are routinely used are the peak gradient strength and the slew rate. Higher maximum gradient power, G_{max}, can be leveraged for high resolution imaging[14]. The slew rate, defined as G_{max} divided by gradient rise time, is a measure of how rapidly magnetic field reaches full power and typically found in the 20-200 T/m/s range[15]. Higher slew rates allow improved temporal resolution for rapid MRI acquisitions (e.g. applications in respiratory imaging or cerebral blood flow imaging). The maximum slew-rate in advanced gradient systems must be considered with reference to existing FDA limits on nerve stimulation or tissue heating, defined in terms of energy per kg of body mass per exposure time. For a full body scan, the figure is 4W/kg/15-minute exposure[18].

Radiofrequency Coils

Two types of radiofrequency (RF) coils required for MR imaging are (i) the RF transmit coil and (ii) the RF receiver coil. In some cases, these two two objects may be combined into one coil called a transceiver coil. For standard clinical MRI systems, the

transmit coil is built into the magnet bore. Its role is to generate RF pulses that cause the homogeneous initial excitation required for MRI signal generation. Receiver coils are usually smaller, more local coils that detect the MRI resonance signal. Receiver coils function based on the principle of Farday's Law of Induction. Changing magnetic flux passing through a receiver coil loop induces an electric current the coil that can be digitized and applied for MR image reconstruction. To minimize external magnetic field interference and reduce the distance between the receiver coil and the tissue to be imaged, specialized receiver coils are often constructed based on the shape of local anatomical regions such as the head, abdomen, or knee joints.

Pulse Sequences and Image Reconstruction

A pulse sequence is a combination of RF and gradient pulses, used to create an MR image with specific contrast. The first step in image acquisition is the application of an RF pulse. In the case of 2D MRI, this is performed in conjunction with slice selection gradients (GSS)[15]. GSS are linearly varying gradients applied at the same time as the RF pulse to image spins at a particular resonant frequency. The imaged slice can be aligned in any orientation along the Cartesian X, Y, Z axes in the magnet frame of reference, or in an oblique orientation.

After the RF pulse and GSS, a phase encoding gradient, GPE, is typically applied in a direction orthogonal to GSS. Application of the GPE results in a spatially dependent accrual of phase along the phase encode direction. After the GPE, application of the frequency encoding gradient, GFE, in the final orthogonal direction results in unique phase for all

protons precessing along the frequency encode axis. GFE activation is also coincident with signal detection in the receiver coil. In 2D imaging, this process is repeated sequentially with N different GPE increments to resolve a 2D slice of the spatial frequency domain with N rows. The process is repeated N times because only one row of phase measurements can be acquired per frequency encode.

The resulting spatial frequency information is often referred to as a K-space image. The K-space representation contains all the image spatial frequencies necessary to reconstruct an image domain representation. The image domain information can be recovered from the K-space data using the inverse Fourier transform.

High Field MRI

The main magnet is generally the most expensive part of the MRI system. Advancements in superconducting magnet technology over the last 20 years have led to the development of human high and ultra-high field MRI systems with field strengths up to 11.7 T[17]. Comparable pre-clinical MRI systems have been produced with field strengths as high as 21 T[19].

Increased main magnetic field strength alters NMR relaxation times, image contrast, and magnetic susceptibility effects. The increased nuclear polarization of protons at high field leads to improvements in SNR that can be leveraged to increase spatial resolution or reduce scan time. For example, 7 T human MRI can now be applied to resolve laminar gray matter myeloarchitechture at the resolution of hundreds of microns[20,21]. This type of imaging

may allow significant advancements in understanding neural processing in the human cerebral cortex.

However, high-field MRI is not without limitations. One notable current limitation of high field MRI is the substantially increased cost associated with the manufacturing of high field MRI systems. Some important benefits and drawbacks of high field MRI are highlighted in the following sections, with an emphasis on comparing 3 T and 7 T MRI in the context of the current thesis.

One overwhelming argument for increasing B_0 strength in MRI is the resulting improvement in signal-to-noise ratio. An often-utilized approach to improve SNR in standard clinical field strength (1.5 and 3 T) MRI is to increase the number of signal averages. SNR improves in proportion to the square root of number of signal averages[15]. However, signal averaging in MRI is time consuming[14]. Since SNR increases linearly with B_0 field strength[22], high field MRI can offer significant advantages for applications requiring high temporal resolution or ultra-high spatial resolution[17]. Improvements in SNR at high field can effectively be "spent" on acquiring images with higher spatial or temporal resolution.

Increased field strength also improves contrast-to-noise ratio (CNR), largely due to changes in the T_1 and T_2 relaxation constants of tissue at the higher fields[14]. Improvements to SNR and CNR have led to breakthroughs imaging cytoarchitecture of the cortical laminae, as well as important developments in cortical BOLD fMRI[23]. CNR improvements in gradient echo MRI at 7 T are mitigated by the shorter T_2^* relaxation of time of tissue at high field. For T_2^*-weighted BOLD fMRI of cortical gray matter, an approximate relationship exists between apparent transverse relaxation rate and main magnetic field strength[24]:

$$R_1 \cong B_0^{-0.7} \quad \textbf{(2.14)}$$

$$R_2^* \cong 10.5 * B_0 \quad \textbf{(2.15)}$$

For gradient echo imaging sequences using TR << T_1 with TE chosen to approximate T_2^*, the CNR can be approximated as[25]:

$$CNR \propto \sqrt{\frac{R_1}{R_2^*}} \cdot \frac{\Delta R_2^*}{R_2^*} \quad \textbf{(2.16)}$$

Where R_2^* represents change in signal between baseline and activated state. Consequently, BOLD fMRI contrast, as well as other T_2^* weighted imaging applications are facilitated at high field[26].

2.2 Brain Physiology

Neurons

The human nervous system, comprised of over 80 billion biological cells called neurons, is predominantly responsible for controlling human physiological processes[1]. Several types of neurons, all specialized for electrical communication are localized in the brain, spinal cord, and peripheral nervous system. This detailed network of neuronal cell bodies plays a critical role in human perception, cognition, and navigation.

The main components of a neuron are the cell body, dendrites, and the axon. The cell body contains the nucleus and ribosomes, required for protein synthesis. Dendrites, typically tens or even hundreds of thousands per neuron, are branched extensions of the cell body and receive incoming signals from neighbouring neurons via chemical neurotransmitters. Substructures attached to dendrites, called dendritic spines, branch out to maximize cell surface area for interactions with neighboring neurons. Electrical signals in the form of action potentials propagate along axons via saltatory conduction[1]. Action potentials are generated at the initial segment of the axon near the the cell body. Propagation of action potentials is facilitated by insulating fatty sheaths called myelin that wrap around the axon.

Action Potentials

The initial segment of a neuron successfully generates an action potential if the sum of electrical potentials from the dendrites exceeds the threshold potential[1]. This mechanism

is governed by selectively permeable ion channels on the neuron membrane. Ion channels gate the flow of charged particles in and out of the cell body to regulate electrical activity. At rest, neurons maintain a net negative potential of roughly -70 millivolts (mV) inside the cell. Electrical stimuli result in the opening of voltage-gated sodium channels accompanied by an influx of sodium (Na+) ions into the neuron and the subsequent depolarization of the neuron. The neuron becomes less negatively charged if enough Na+ ions enter the neuron and it depolarizes at a critical threshold potential, typically -55 mV. A positive feedback loop initiates among all Na+ channels, causing a voltage rise of up to 100 mV. This overshoot triggers a brief period of net positive charge in the intracellular compared to the extracellular compartment, resulting in the opening of potassium (K^+) channels and rapid outflux of potassium. This action returns the polarization state of the neuron to equilibrium. The potassium channels close relatively slowly, causing excess K^+ ions being lost and a small hyperpolarization effect. Lastly, a special protein called the Na+/K+ATPase, which exports 3 Na^+ ions for every 2 K^+ ions imported, brings the cell voltage back to its -70 mV equilibrium.

White Matter and Axons

Axons are long fibers varying from mere millimeters to a meter in length in the human body. The propagation of action potentials along axons is mitigated by three main structures: the axon itself, the myelin sheath and the nodes of Ranvier.

The overall speed of action potential propagation depends on the axon diameter. This diameter partially determines the resistance to electrical current and the extent of ion influx

upon depolarization. Humans axon diameters are typically 1 micrometer[1]. The myelin sheath surrounding axons is a lipid-rich structure that provides insulation and enables that saltatory conduction of axon potentials. Regularly occurring unmyelinated sections of the axon, called nodes of Ranvier, are lined with sodium channels. The nodes of Ranvier generate/propagate action potentials by using a positive feedback loop. In this sense, it is technically more accurate to describe signal propagation along the axon as a regeneration of action potentials at each consecutive node of Ranvier. Action potentials propagate at an average speed of 0.5-100 meters per second in humans. However, the speed of action potential propagation depends on axonal diameter.

Myelinated axons in white matter of the brain comprise around 60% of brain parenchymal tissue volume. Gray matter, forming the outer cortex and deep brain nuclei, comprises the remaining 40% of parenchymal tissue. Gray matter neurons are connected by a highly structured network of white matter axons, called tracts. In many ways, the brain structure can be compared to a computer where gray matter forms computational processing sites, connected by the intricate wiring of the white matter.

Gray Matter and Neurovascular Coupling

Gray matter is primarily comprised of neuronal cell bodies. External stimuli in the brain reach gray matter via sensory neurons and the spinal cord. The spinal cord processes information and then sends instructions to the peripheral nervous system to manage physiological function and cognition. “Activation” of gray matter occurs in conjunction with

cellular consumption of oxygen. The brain itself does not store energy reserves. It relies on cerebral blood flow (CBF) to supply oxygen and nutrients. During early MRI experiments, it was observed that increased neuronal activity led to increased local oxygenation—a paradoxical result because oxygen should be consumed to feed neural activity. Fox and Raichle specifically showed, using Positron Emission Tomography imaging, that an "uncoupling" occurred between physiological oxygen demand and blood flow[27]. That is, that regional CBF increased, but the metabolic rate of cerebral oxygen consumption did not. The interpretation of this finding was that oxygenated blood was oversupplied locally compared to actual metabolic needs. As oxygen saturation increases in the capillaries, accelerated diffusion rate-limited delivery of oxygen for neuronal function occurs. This results in elevated BOLD signal in fMRI due to elevated deoxyhemoglobin causing T_2 and T_2^* shortening effects. The shortened T2 and T2* signal is a proxy for neuronal activity[15].

Functional Neuroimaging

The MRI-detectable, T_2^*-weighted BOLD signal change is less than 2% of the baseline signal observed in gradient echo MRI. For this reason, the methodology used in fMRI must be highly sensitive and accurate. Several factors can compound measurement error in fMRI, including signals from venous circulating blood, respiration, large-scale subject movement, and interference from physiological measurement devices. Optimized fMRI experimental design can minimize physiological noise and is of vital importance in isolating the true BOLD signal.

Traditional fMRI experiments used task-based paradigms to induce BOLD signal changes in selected brain regions. For example, a subject might be presented with an auditory stimulus or instructed to tap a finger in order to elicit a BOLD response[28]. This localized BOLD signal change in task-based fMRI has traditionally been modelled using a characteristic pattern with a small initial dip, succeeded by a rise. This is then followed by a drop to below initial baseline, and a subsequent return to baseline. This pattern is known as the hemodynamic response function (HRF). However, the traditional view of the HRF shape has recently been challenged by studies of the HRF variance based on brain matter composition (WM and GM), cortical depth, and other factors. More specifically, HRFs may be regionally-specific in the brain and not exhibit an initial dip[29]. Nonetheless, the shape of the HRF can be explicitly modelled into task-based fMRI studies.

In 1995, Biswal et al. discovered the existence of intrinsic functional brain activity after scanning subjects at rest[30]. The resulting BOLD fMRI measurements revealed surprising correlated activity between different regions of the sensorimotor system. Major progress was further made in 2001, when Raichle et al. identified the existence of the "Default Mode Network" (DMN) in subjects who were scanned at rest[31]. The DMN demonstrated active and correlated neural activity between the medial prefrontal cortex, posterior cingulate cortex and the adjacent precuneus, leading to the hypothesis of a "default mode" of brain activity.

MRI scanning of subjects at rest places less demand on the subject (compared to task-based fMRI) while maintaining the potential to collect valuable data related to gray matter function. For instance, patients having difficulty following instructions caused by brain

injuries can be scanned without requiring case-by-case experimental designs. Accordingly, rsfMRI has experienced an explosion in usage since the early 2000's in nearly all areas of neuroscience. Since the first discovery of the DMN in 2001, at least a dozen robust and highly reproducible resting state networks have been identified and well-studied in both humans and animals[32,33].

How and why the brain organizes into characteristic networks of functional activation is not well understood. Nonetheless, comparing patterns of functional connectivity between subjects highlights interesting results. Recent studies have used rsfMRI to illustrate increases in whole-brain functional connectivity (FC) in certain pathological conditions. Increases in FC have been observed in the elderly with subjective memory complaints[34] and in Alzheimer's Disease[35]. Decreases in FC may be associated with aging[36] and depression[37]. Nonetheless, in most pathological conditions prevailing literature suggests a combination of both increases and decreases in inter-regional brain FC exists, including multiple sclerosis[38].

Blood-Brain Barrier and Cerebrospinal Fluid

Cerebrospinal fluid (CSF) and blood flow are vital for supporting healthy brain function. Oxygen and nutrients enter the brain through the arterial circulation from the heart. Transport of important molecules such as nutrients and hormones to the brain tissue occurs through specialized transport proteins in the blood-brain barrier (BBB). The BBB is a semipermeable membrane separating circulating blood from the extracellular fluid. It is a

highly selective barrier composed of tight junctions of endothelial cells having their own associated subunits, making it the brain's primary defence against pathogens, blood infections, and other large molecules.

CSF circulates both outside the brain and within the brain's ventricular system. The ventricular system has four large cavities, each containing a choroid plexus that produces CSF. CSF produced by the choroid plexus is a clear, colorless fluid having several vital roles in the brain: physical cushioning and buoyancy support, regulation of cerebral blood flow (CBF) and flushing of waste back into the bloodstream. At any given time, roughly 125ml of CSF flows throughout the brain and spinal cord, while 500ml of CSF is produced per day[1]. CSF is separated from the circulatory system via the blood-cerebrospinal fluid barrier (BCFB), which works like the BBB in principle, in that it protects the nervous system from undesirable large molecules. Structurally, the BCFB is not as tight, allowing more molecules into the bloodstream. This is important for sustained CSF production from the choroid plexuses.

Neurological disorders often affect WM, GM, CSF, and the BBB in an inter-related manner. This is particularly apparent in multiple sclerosis, where white matter damage is prevalent, but pathophysiological markers of neuroinflammation and neurodegeneration also exist in the GM, CSF and BBB.

Physiology of Multiple Sclerosis

MS is an autoimmune disease that results in inflammation of the central nervous system and damage to axonal myelin sheaths in the brain. Three prevalent categories/phenotypes of MS are recognized in the clinical literature and account for over 95% of cases[3]. Relapsing remitting MS (RRMS) is by far the most common phenotype and accounts for 85% of initial diagnoses. It is characterized by episodes of dysfunction, alternating with periods of stability which may be associated with worsening of symptoms. Usually 5-10 years after the onset of RRMS, Secondary progressive MS (SPMS) follows. This phenotype is characterized by a progressive worsening of the disease without signs of recovery. Primary Progressive MS (PPMS) is the third major MS phenotype, in which the disease gradually and continuously worsens from onset. PPMS accounts for 10% of cases. A fourth group, Clinically Isolated Syndrome (CIS – distinct from MS) refers to patients who have experienced a single episode of MS-like symptoms. CIS patients may or may not be diagnosed with MS in the future.

Currently, there is no known cause or cure for MS. However, there is strong evidence that geographical and genetic factors play a role. For example, the country with the highest prevalence of MS is Canada, having nearly 400 cases per 100,000 people. Canada is followed by a number of European countries which are geographically located between 45 degrees and 65 degrees in latitude[39]. Countries along the equator have the lowest prevalence of MS[40].

No genetic risk factors for MS have been definitively isolated. Nonetheless, it is known that females are disproportionately more likely to develop MS compared males. The

worldwide female-to-male incidence rate of MS is 3:1[41]. People of Northern European descent are also among the highest risk groups[42].

In recent decades diagnostic techniques have vastly improved the MS diagnosis. They have concurrently aided to improve life expectancy and quality of life of MS patients. Some patients can achieve equal life expectancies to the normal population and have more limited disability. Disability in MS is assessed by a clinical neurologist and often quantified according to the Expanded Disability Status Scale (EDSS)[43]. The EDSS score measured by a neurologist during a patient clinical visit varies from 0 to 10, incrementing in units of 0.5. RRMS patients generally have lower scores on the EDSS scale (0 to 4.5), while SPMS patients often have disability scored at 5 or above.

EDSS scores are assigned based on sub-scores measuring impairment across eight functional systems (FS), where each FS is a network of brain regions responsible for a type of task. The eight systems in MS are: pyramidal, cerebellar, brainstem, sensory, bowel and bladder, visual function, cerebral function, and “other”. The EDSS scoring system is summarized in table 2.2.

EDSS SCORE	DESCRIPTION
0	No disability.
1.0	No disability and minimal signs in one FS.
1.5	No disability and minimal signs in more than one FS.
2.0	Minimal disability in one FS.
2.5	Minimal disability in two FS.
3.0	Moderate disability.
3.5	Moderate disability in more than one FS. Does not require walking assistance.
4.0	Relatively severe disability in one FS or equivalent. Does not require walking assistance.
4.5	Able to work full day. May require some assistance day-to-day due to severe disability in one FS or moderate disability in multiple FS. Able to walk without aid or rest for 300 meters.
5.0	Disability impairs daily activities. Able to walk without aid or rest for 200 meters.
5.5	Disability impairs or fully precludes daily activities. Able to walk without aid or rest for 100 meters.
6.0	Requires unilateral aid to walk 100 meters without rest (cane, crutch, etc.)
6.5	Requires bilateral assistance to walk 20 meters (canes, crutches, etc.)
7.0	Unable to walk for more than 5 meters. Reliant on wheelchair for most transport.
7.5	Unable to walk for more than a few steps. Reliant on wheelchair for most transport.
8.0	Confined to bed or wheelchair. Generally self-reliant.
8.5	Confined to bed. Able to care for self mostly.
9.0	Confined to bed. Dependent for care. Can eat and communicate.
9.5	Confined to bed. Fully dependent for care and unable to eat and swallow Unable to communicate effectively.
10	Death due to MS.

Table 2.2: Expanded Disability Status Scale (EDSS) score with corresponding description of symptoms. The table is adapted from the original scoring criteria developed by Kurtzke[43].

Axonal White Matter Damage

The first detailed work studying white matter lesions in MS was completed by physicians Jean-Martin Charcot and Edme Vulpian in 1868[44]. They built on the previous works of Robert Carswell in 1838 and Jean Cruveilhier in 1841, both of whom independently observed discolorations and scarring in the white matter of brain and spinal cord tissue. Furthermore, the two specifically identified patterns of lesions associated with CNS impairment and a resulting "triad" of symptoms—unsteady eyes, impaired speech, and loss of motor coordination. The presence of lesions combined with this triad of symptoms which they named "sclerose en plaque disseminee" eventually becoming known as "multiple sclerosis" [44].

Lesions arise from demyelination of white matter axons which then appear as discolorations in neural tissue when the characteristic light color of myelin is absent. At the cellular level, the myelin sheath function is to insulates action potentials travelling through the axon from the extracellular matrix and speed up its conduction velocity[1]. Loss of the myelin sheath thus slows down conduction, disperses action potentials into the extracellular space, or may even block action potentials altogether. Subsequent inability of neurons to communicate properly between the brain and spinal cord may lead to the beginning of physical and mental dysfunction.

The location and distribution of WM lesions has seen increased understanding in recent years with knowledge advances in imaging and immunology. In a study by Charil et al, some relationships were found between lesion location and cognitive and motor

disabilities. Specifically, presence of lesions at the gray-white matter junction correlated with cognitive impairment, while lesions near the lateral ventricles and internal capsule were associated with motor impairment[45]. This finding should be taken in context with the well-recognized clinico-radiological paradox, which describes a lack of correlation between MS disability and total white matter lesion burden[46]. The EDSS itself is also biased towards motor disability. Other clinical disability scores have recently been proposed, including the Multiple Sclerosis Functional Composite (MSFC), which incorporates cognitive testing[47].

During the transient, stable periods of RRMS axonal remyelination may occur[48]. However, complete remyelination never occurs[49]. SPMS, as well as PPMS are characterized by progressive increases in demyelination and axonal loss. They are also linked to a lower capacity of the brain to remyelinate damaged axons[50].

Gray Matter Pathology in MS

There are substantial changes in cortical and subcortical GM in MS. Early studies by Brownell et al. showed that 26% of lesions in MS are localized in the cortical and subcortical GM[51]. This finding was later corroborated by Kidd et al in 1999[51]. Kutzelnigg et al. subsequently studied MS lesions in post-mortem tissue and reported more extensive GM lesions in the cortex in PPMS and SPMS subjects compared to RRMS[52]. Furthermore, demyelination GM has been identified in deep GM nuclei including the basal ganglia, cerebellum, thamalus, hypothamalus, as well as in the cerebellum[51,53].

Despite its reported prevalence in histopathology studies, cortical GM pathology in MS is difficult visualize using MRI for several reasons: (1) GM lesions are smaller than WM lesions in size and (2) there are smaller differences myelination between GM lesions and surrounding normal-appearing gray matter[3].

Signatures of GM pathology in MS can be identified based on MRI atrophy measures. For instance, Fisher et al. 2008 demonstrated that GM atrophy increases 14-fold in SPMS compared to RRMS, while WM atrophy remains the same[54]. This finding indicates the more pronounced brain parenchymal tissue loss (which is visible in MR images) in progressive MS is primarily a function of GM atrophy. A relationship between GM atrophy and disability has also been demonstrated by Fisniku et al.[55].

Functional Disruptions in Multiple Sclerosis

In one of the earliest fMRI studies of MS, Rombouts et al. examined MS patients with unilateral optic neuritis compared to a group of healthy controls[56]. After stimulating each eye, subjects with optic neuritis showed decreased activation in the affected eye. They also showed decreased activation in both eyes compared to controls. In subsequent years, task-based fMRI studies have elucidated important functional changes in MS brain. Werring, et al, showed that MS subjects who recovered from optic neuritis displayed overall changes in their distribution of cortical activation[57]. Prior to recovery patients displayed visual activation in the occipital visual cortex. After recovery, the activated sites also included the

insula-claustrum, lateral temporal cortex, posterior parietal cortex, orbital prefrontal cortex, corpus striatum, and the thalamus.

Compensatory cortical activation in the presence of lesions in has also been observed in early stage MS. In 2002, Staffen et al. demonstrated the existence of increased cortical activation in RRMS patients compared to controls[58]. In the study, in neuropsychological testing of memory and attention, healthy controls and RRMS subjects showed no group differences in any of the test scores. However BOLD activation was markedly different. Healthy controls had increased activation in the right frontal gyrus cingula. RRMS subjects had increased activation in a wider range of areas, including Brodmann areas 6, 8, and 39 in the right hemisphere, as well as Brodmann area 39 in the left hemisphere. A later study also highlighted increased prefrontal cortex activation in RRMS[59] during the Stroop test[60], a test of matching colors with mismatches words, where MS and control groups had statistically insignificant test differences. Such results further extend to motor tasks. Two notable results include increased contralateral supplementary motor area activation in fatigued MS patients compared to non-fatigued and HC subjects during finger flexion-extension tasks[61], and in PPMS patients compared to controls in an ankle flexion task, higher activation in a network of regions that is normally associated with tasks of higher complexity level[62].

Several novel technologies and methods were introduced in the early 2000's and saw applications in MS research. Among these developments were more powerful magnets to elucidate deep subcortical structures, and the discovery of resting state networks to explore FC changes[63].

Exploration of resting state networks has unveiled important FC changes, especially in the default mode network, visual network, and sensorimotor network[38]. In the DMN, the posterior cingulate cortex and anterior cingulate cortex, two major network hubs, have shown decreased FC in PPMS and SPMS[64] and RRMS[65]. However, there is also evidence of FC increase between in PCC and ACC of the DMN in RRMS subjects[66]. In the visual network, RRMS and CIS has consistently seen decreases in FC[67–69], possibly due to higher susceptibility to structural damage[70]. Lastly, sensorimotor network sees decreased FC between nearly all connections in RRMS, particularly at the premotor cortex[71], postcentral gyrus[72] and thalamus[73].

The link between FC changes and structural changes such as recovery and compensatory alterations is not fully understood. Intuitively, one might think compensatory activation in formerly unrecruited brain regions may be advantageous, but evidence has arisen that compensatory changes in functional activation may be short-lived, unsustainable, and even detrimental in the long term. For example, in two studies of PPMS subjects, Filippi et al. showed correlations between widespread compensatory motor activation linked to later detrimental structural evolution[74]. Second, Pantano et al. showed, in a longitudinal study of 15-26 months between scans, that RRMS patients showed initially higher bilateral activation than controls. In the follow-up scan, after increased lesion load and relapse in the RRMS group, BOLD activation reduced significantly in the ipsilateral sensorimotor cortex and contralateral cerebellum[75].

3. Methodology

3.1 Study Overview

As the primary research objective of this thesis, we sought to isolate the influence of MS phenotype on local and global resting-state functional connectivity in a cohort of early and later stage MS patients. All subjects were imaged using the 7 T MRI system located at the Robarts Research Institute in London, Ontario.

Resting state network activation patterns in MS are regionally-specific and may exhibit either increases or decreases in activation. However, a conceptual understanding of what governs such resting state alterations is lacking. Moreover, associations between FC and structural-MRI derived signatures of neuroinflammation and neurodegeneration are not fully understood. Herein, we aimed to quantify 7 T-derived, resting state fMRI (rs-fMRI) alterations at the network level in relapsing-remitting and secondary-progressive MS patients compared to age, sex and education-matched healthy controls.

3.2 Subject Recruitment

RsfMRI data was collected as part of an ongoing study of cortical pathology in MS which is being conducted jointly between McGill University and University of Western Ontario. The imaging portion of the study includes 40 subjects who were imaged on the 7 T MRI system at the University of Western Ontario. The cohort distribution was as follows: 15 Healthy

Controls (HC), 14 Relapsing-Remitting MS (RRMS), and 11 Secondary Progressive MS (SPMS) subjects. By sex, there were 14 males and 26 females in the study.

3.3 Neurological and Cognitive Testing

Neurological assessment of each MS subject was performed by a board-certified neurologist at the London, Ontario MS Clinic. Each patient was assigned an Expanded Disability Status Scale (EDSS) score. This is discussed in section 2.2. Values for EDSS for subjects enrolled in our study ranged from 0 (no disability) up to 6.5 (requirement of two walking aids to walk 20 meters without rest). Subject EDSS Scores are summarized in Appendix X.

In addition to clinical neurological evaluation, each subject underwent cognitive testing. The cognitive testing battery included:

- Leonard Tapping Test (LTT), which evaluates motor coordination of two hands using a two-circle apparatus, each divided into four regions[76]. The left and right circles of the apparatus correspond to the left and right hand of the subject. Test takers are required to tap regions of each circle in the correct order. Specific tests included single tap, sequential tap, bimanual in-phase tapping, and bimanual out-of-phase tapping. The final score for the LTT is an average of the number of correct taps in all tests, with separate scores assigned for the dominant and non-dominant hand.
- Symbol Digit Modalities Test (SDMT), a test designed to measure processing speed through identification of symbol and digit associations, and the most frequently used

neuropsychological test for this purpose in MS[77]. Symbols and associated numbers are defined. Subjects are then asked to correctly identify as many correct matches as possible in 90 seconds. Scores are recorded for the correct number of associations. They are then scaled to Z-scores based on a population average.

- Wechsler Adult Intelligence Scale, 3rd edition (WAIS-III), designed for testing IQ in adults[78]. In the current study, data is available for the processing speed tests associated with WAIS-III which includes a digit symbol-coding test, similar in principle to SDMT where subjects match numbers to symbols, and a symbol search test, where subjects identify if a given pair of symbols exist within a larger set of symbols. In both subtests, the number of correct responses is recorded in a set period, and scores are scaled into percentiles.
- Beck Depression Inventory 2nd edition (BDI-II), a set of 21 self-scored questions about feelings over the past two weeks at the time of questionnaire[79]. Individual responses are rated from 0 to 3, and the final sum (BDI-II score) ranges from 0 (normal/non-depressed) to over 40 (extremely depressed). The questionnaire and scoring system for BDI-II is included in Appendix X.
- Modified Fatigue Impact Scale (MFIS), a set of 21 self-scored questions, rated from 0 to 4, relating to recent events in relation to fatigue[80]. The sum of the results from selected individual questions contributes to a physical, cognitive, and psychosocial sub-score. The total score is the sum of scores from all responses which generates the final fatigue score ranging from 0 (non-fatigued) to 84 (severe fatigue). The questionnaire and scoring system for MFIS is included in Appendix X.

- Tower of London 2nd edition (TOL-2), a psychological test designed to assess executive function[81]. In this test, three towers are presented, in which a red, green, and blue ball are stacked in a starting configuration. The configuration is first presented by the examiner, and the subject attempts to re-create the configuration as fast and efficiently as possible. Efficiency is judged by number of moves necessary to re-create the configuration. A score is derived by calculating the difference between the number moves used and the optimal number of moves (i.e. move score of 0 means perfect sequence of moves). Speed is also judged based on initiation time (time taken to plan), and execution time (time taken to execute the plan). Move score and time score are combined and scaled into percentile performance scores for each subject.
- Paced Auditory Serial Addition Test (PASAT), which assesses auditory information processing and mathematical calculation ability[82]. The subject is first presented with a number, delivered from an audio cassette or disk. In regular repeating intervals of time, a digit is presented, and the subject must add the digit to the previously presented digit, thus requiring holding the previous digit in memory. A total of 60 digits are presented with 2-second and 3-second intervals between digits are tested in the PASAT-2 and PASAT-3 tests, respectively. The final number of correct answers is scored and scaled to give a z-score based on population average statistics.

A full summary of patient EDSS information and cognitive testing parameters is presented in appendix X.

3.4 Imaging Protocol

Each patient underwent a 7 T human MRI scan on the Siemens MAGNETOM MRI system at the Centre for Functional and Metabolic Mapping of the Robarts Research Institute in London, Ontario. The scanner is specialized for neuroimaging applications and has a clear magnet bore of 680 mm. Further, it is equipped with a 32-channel receive head coil and imaging gradients that can achieve a maximum amplitude of 80 mT/m with a 350 mT/m/s slew rate.

Each subject enrolled in our study underwent a T_1-weighted structural MRI using a Magnetization Prepared 2 Rapid Acquisition Gradient Echoes (MP2RAGE) pulse sequence with 0.7 mm^3 spatial resolution. Functional rsfMRI data were subsequently acquired using a multi-band EPI sequence with 10-minute acquisition window to collect 480 total image volumes. The spatial resolution of the rsfMRI scan was 2 mm^3. Subjects were instructed to remain awake throughout the duration of the scan. Neck and head cushions were provided to minimize patient movement. Imaging parameters are detailed in table 3.1 and 3.2, respectively.

Acquisition Parameters:			
Multislice Mode	Interleaved		
Slices Acquired	224		
PAT Mode	GRAPPA		
Acceleration Factor PE	3		
PE Direction	A>>P		
TR	6000 ms		
TE	2.73 ms		
Orientation	**Direction**	**FOV**	**Slices**
Sagittal	R >> L	240 mm	342
Coronal	A >> P	240 mm	342
Transversal	F >> H	157 mm	224

Table 3.1: 7 T MP2RAGE acquisition parameters that were employed for anatomical imaging in our study.

Acquisition Parameters:			
Multislice Mode	Interleaved		
Slices Acquired	56		
PAT Mode	GRAPPA		
Acceleration Factor PE	2		
PE Direction	A>>P		
TR	1250 ms		
TE	18.0 ms		
Total scan time	600 seconds		
Total volumes acquired	480		
Orientation	**Direction**	**FOV**	**Slices**
Sagittal	R >> L	208 mm	104
Coronal	A >> P	208 mm	104
Transversal	F >> H	124 mm	56

Table 3.2: 7 T Echo Planar Imaging (EPI) parameters applied for BOLD fMRI.

3.5 MRI Preprocessing

Preprocessing for our study consisted of two major steps: (1) extraction of the BOLD timeseries signal from raw T_2^*-weighted functional MR images, and (2) alignment of subject brain volumes to a 3D standardized space for group-level analysis.

Registration Procedure

Anatomical Cortical Parcellation

As a preliminary step in our analysis, tissue classification using the FreeSurfer[83] pipeline was applied to 7 T, T_1-weighted structural MR images. This was carried out to classify tissue structures, extract cortical volume and measure cortical thickness. Brain parcellation was accomplished using Freesurfer's registration procedure to a target atlas optimized for cortical folds[84]. The atlas contains probabilistic labels for brain regions and structures[85]. Thickness measurements were computed using second order smoothing of vertex-wise mesh of the white and pial surfaces[86].

T1-weighted Brain Extraction

Prior to subject registration, a brain extraction was performed using the T_1-weighted anatomical image. This step removed the skull and surrounding non-brain tissue. In the current study, the BET2 algorithm[87], included as part of the FSL software package[88], was

used for brain extraction. BET2 first analyses the pixel intensity distribution in the T_1-weighted image. It then calculates a brain/background threshold in order to estimate the approximate position of the center of gravity of the brain. In these calculations, the top and bottom 2% of pixels are removed to minimize the effect of outliers due to MRI system-specific parameters and brightness from arterial blood. Bone is also treated as background by setting the brain/background threshold to 10% between lower and upper intensities. Next, a brain radius is roughly estimated based on voxels above the threshold intensity. This radius is employed to tessellate a spherical surface which approximately matches the brain surface. An iterative procedure then more precisely estimates the brain surface by modifying each vertex on the sphere incrementally until an optimal solution is found.

In practice, several changes were made to the default BET2 algorithm to accommodate the high resolution (0.7 mm^3 isotropic voxels) T_1-weighted images (based on the MP2RAGE uni-den contrast) from our 7 T acquisitions. First, because the T_1-weighted images contained non-brain tissue—fat, muscle, and skin—around the neck which show up bright in T1 images, the center of gravity estimates used by the brain masking algorithm were rendered less accurate. To address this issue, a "robust" brain center estimation was carried out. Briefly, the estimate procedure iterates the BET2 brain extraction process using updated center of gravity information at each iteration. The iterations will stop when the center of gravity no longer changes (within a tolerance threshold).

The fractional intensity threshold employed in the BET2 algorithm determines edge of the final brain mask segmentation. The threshold is controlled manually and varies from 0 to 1, where larger values lead to smaller final brain size estimates. The default option in

BET2 is 0.5. For the 7 T images in our study, this threshold resulted in excessive removal of brain tissue. A fractional intensity threshold of 0.1 was found to be optimal based on visual inspection.

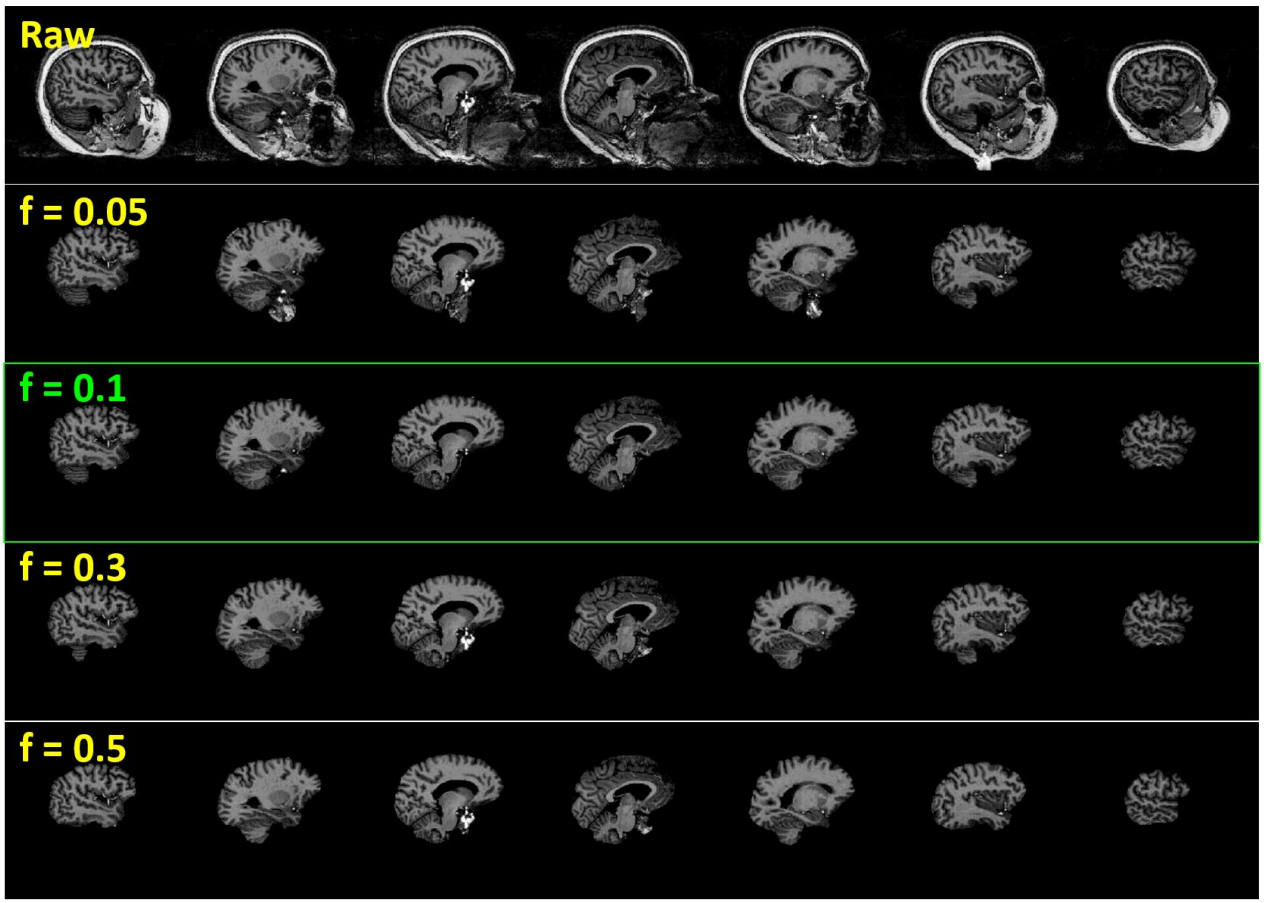

Figure 3.4: Visual comparison of MP2RAGE uni-den images and the effect of varying levels of BET2 brain extraction, fractional intensity threshold. The threshold value affects how much cortex is preserved. Values below 0.1 left too much tissue, while values above 0.1 did not adequately remove non-brain tissue.

A final step to refine the brain extraction involved a gradient in the BET2 fractional intensity threshold (from the top to the bottom of the image). The gradient ranged between -1 and +1. A positive value of gradient resulted in more tissue eroded at the top half of the image. For the brain extraction performed based on the 7 T MP2RAGE images of our MS

imaging study, the gradient threshold was iteratively adjusted in intervals of 0.1 between -0.3 and +0.3. The optimal removal of non-brain features was judged by visual inspection.

Registration to Standard Space

Registration from functional MRI space to a template atlas requires calculation of a transformation/registration matrix. The transformation matrix was computed using an iterative algorithm based on the high-resolution, skull-stripped T_1-weighted data. The final registration target was the Montreal Neurological Institute 152, 2mm atlas (MNI_152_2mm)[89].

Detail regarding the specific registration procedure is given below:

Step 1: Segment the T_1-weighted brain image into white matter and gray matter. This was accomplished using the FMRIB's Automated Segmentation Tool (FAST)[90] which utilizes a hidden Markov random field model (MRF) with an expectation-maximization (EM) algorithm to label pixels contextually, constrained by spatial information from neighboring pixels (Zhang et al 2001). The algorithm begins, with an input skull-stripped image. A three-step EM algorithm is then applied iteratively using the MRF and maximum-likelihood estimates to calculate class labels and tissue parameters. Furthermore, the FAST algorithm estimates global bias fields/image non-uniformity and can remove it from the image.

Step 2: Linear boundary-based registration (BBR) to register functional MR image to the high resolution, T_1-weighted structural[91], included in the FSL package as the "epi_reg"

function. BBR requires a high quality, segmented reference image. In our case, the reference image was obtained from step 1. BBR also qualitatively requires that the functional MRI data, have strong tissue contrast. Boundary-based alignment is achieved by computing a maximum gradient of the input image intensities across a segmented white matter surface[91]. The output of the registration procedure is a 4x4 affine transformation matrix.

An alternative registration algorithm explored as part of this thesis was FMRIB's Linear Image Registration Tool (FLIRT)[92,93]. In theory, approximate registration of two MRI contrast from the same subject, scanned in the same session should be achievable with linear affine registration using the FLIRT tool. However, in practice, final alignment of 7 T fMRI data to high resolution T_1-weighted images with FLIRT was sub-optimal and BBR proved to be more consistent. The improvement registration achievable with BBR may be a result of its unique ability to compensate for the effects distortion in the 7 T fMRI data.

Step 3: A non-linear transformation field was computed to register the high-quality reference T_1-weighted image to the final MNI_152_2mm atlas space for group statistical analysis. This step was achieved using the Advanced Normalization Tools (ANTs) package[94]. ANTs performs nonlinear registration in a step-wise manner. First an approximate, rigid body transformation (shifting and rotating only) is estimated for rough alignment. This is followed by affine registration (shearing and scaling), then application of the Symmetric Normalization (SyN) algorithm[95] for nonlinear registration to atlas space.

The SyN nonlinear registration, allows for finer detail and control than affine linear registration for small and detailed structures in the brain such as sulci and gyri, while also being able to correct larger features like ventricles that may be present in highly atrophied

brains. SyN is fundamentally a based on diffeomorphic transformation, which means reference and input maps are treated as closed and differentiable with a differentiable inverse. One can visualize the surfaces as being smooth, and some of the resulting mathematical implications are that the solutions in image registration are well behaved and constrained in terms of their distance and change, and topology of the reference image is preserved.

The resulting output from ANTs is a deformation field represented by a 3D transformation matrix.

Step 4: In a final step, the calculated transformations from step 2 and 3 were applied to the functional MRI data to align it with the T_1-weighted anatomical data using the linear transformation matrix from step 2. This was followed by application of the nonlinear deformation field calculated from step 3 to sensitively align the fMRI data to the MNI_152_2mm atlas space.

The entire registration procedure is summarized in figure 3.6.

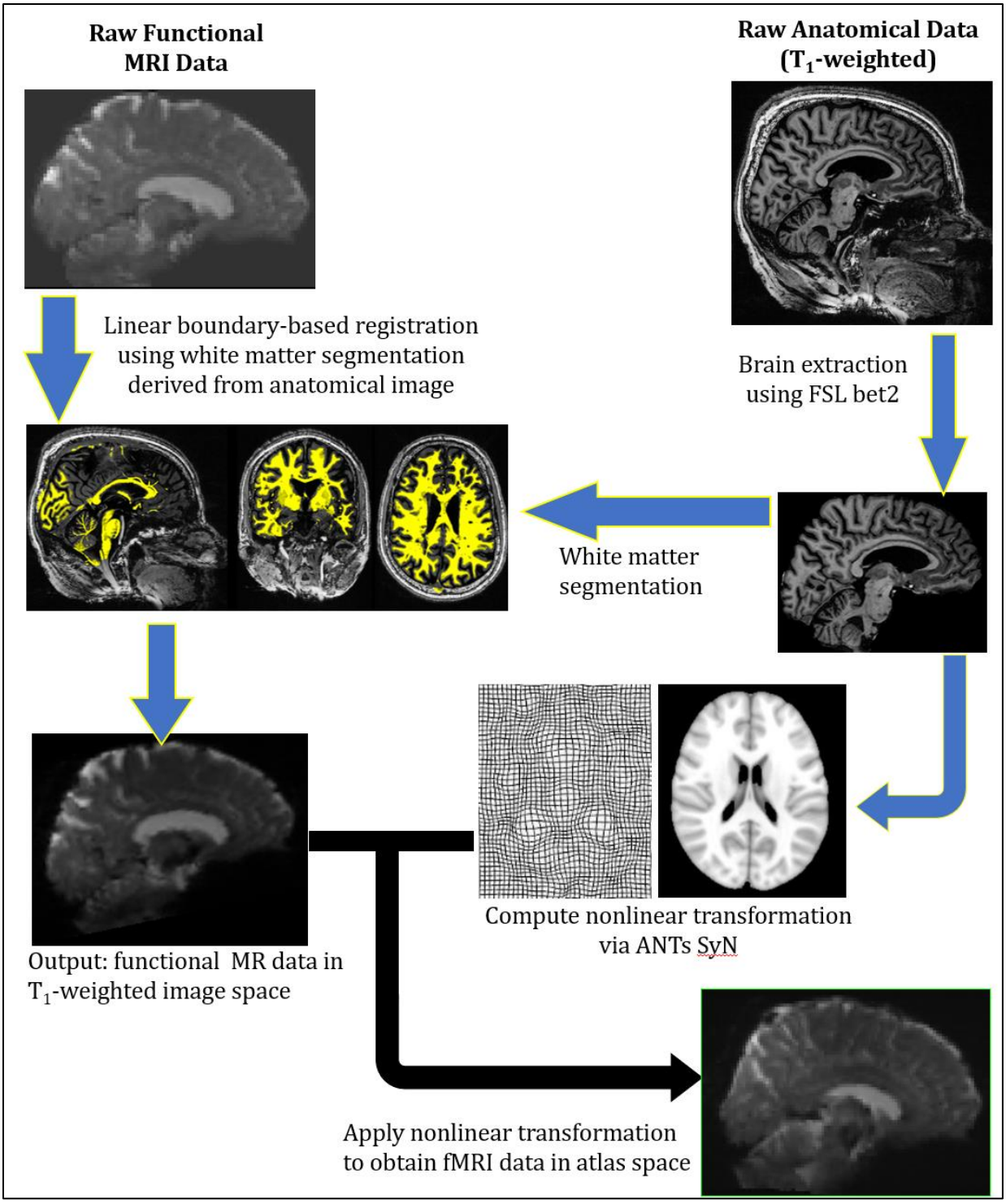

Figure 3.6: Summary of the multi-step, image registration pipeline employed in our study. Raw fMRI data (top left) undergoes BBR with the aid of WM segmentation via FSL FAST Algorithm on the high quality T1-weighted anatomical data (top right). Furthermore, T1-weighted data is registered to MNI152 2mm atlas via ANTs SyN algorithm to compute a nonlinear warp field. The fMRI data that was transformed to T1-weighted anatomical space (bottom left) is then subject to the nonlinear warp field to produce the final registered fMRI image in atlas space.

Functional Preprocessing

Artefact removal was performed based on the registered 7 T functional MRI data using a series of FSL preprocessing tools. Key steps in artefact removal are explained in the following sections.

In this resting state fMRI data, BOLD signal is acquired in every voxel in the brain every 1.25 seconds. Resting state networks were specifically evaluated in cortical and subcortical regions that displayed coherent signal fluctuations over the 10-minute duration of the scan. Physiological processes such as breathing, venous and arterial blood flow, and voluntary or involuntary head motion can result in artefactual, correlated BOLD signal. Furthermore, variations in MRI system parameters such as gradient heating can cause artificial gain or loss of signal locally or globally. These non resting state network (non-RSN) signals must be removed from functional images in order to ensure that the data contains real and relevant signal.

Specialized pre-processing was applied to remove artefactual respiratory and cardiac signals from the raw rsFMRI data. In particular, single-subject independent component analysis (ICA)[96]. was applied as an artefact removal step.

Motion Correction

The motion correction algorithm, motion correction FLIRT (MCFLIRT)[92], was applied in our study to remove functional magnetic resonance image volumes corrupted by

significant head motion. During the 10-minute fMRI scan, 480 total volumes are acquired, and two measures of motion were be considered: absolute head motion (absolute position of the head throughout the course of the scan) and relative head motion, (head displacement occurring in any given volume compared to the next volume which was acquired 1.25 seconds later).

Absolute head motion was corrected by using the middle volume as a reference and applying MCFLIRT to realign volumes before and after the reference point. The MCFLIRT algorithm compares image intensities and uses a normalized correlation cost function for volume alignment.

Relative head motion between fMRI volumes is a greater challenge because. Large inter-volume movements can cause artificially spurious correlations in BOLD activity throughout the entire brain which may outweigh actual resting state activity[97]. In the current study, the MCFLIRT algorithm computed both relative and absolute motion in the time series data. Relative motion greater than 0.9 mm between volumes was identified for each subject and a confound matrix was created to discriminate corrupted from non-motion corrupted volumes. Specifically, the confound matrix was read into the fsl_motion_outliers tool[98] of the FSL package to remove unwanted signal contributions from outlier volumes.

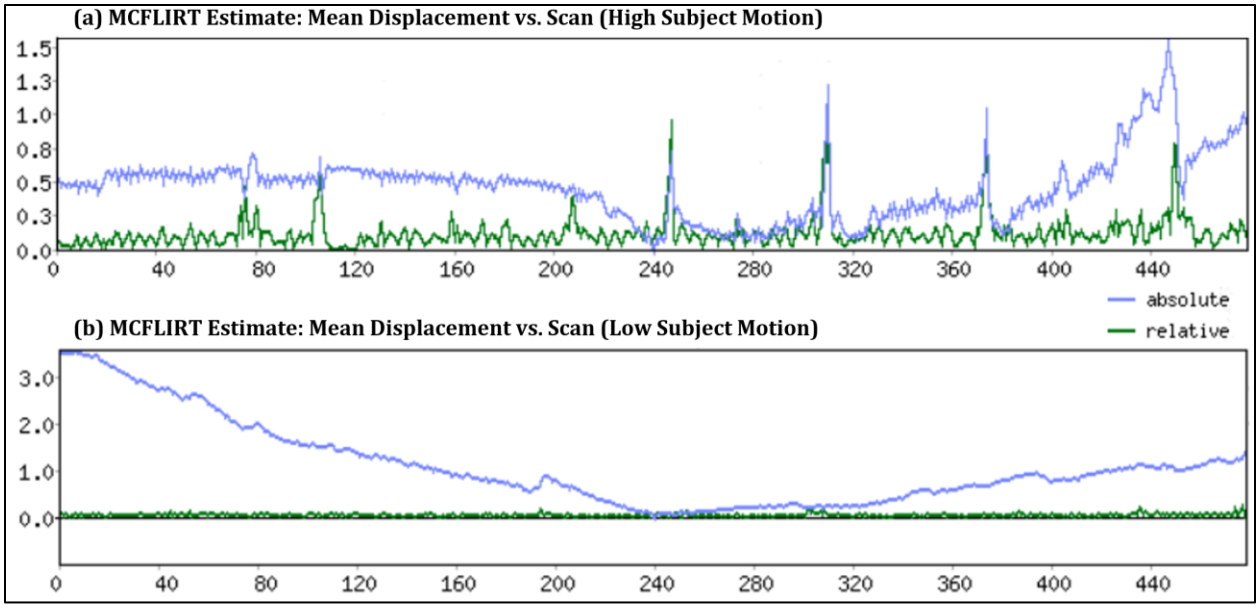

Figure 3.7: Examples of (a) high subject motion and (b) low subject motion artefact in two selected fMRI scans. Relative displacement refers to the net displacement between volumes at successive time points. Absolute displacement refers to the relative displacement compared to the center volume (n=240).

Slice Timing Correction

Slice timing correction refers to the mitigation of temporally misaligned slices due to the chosen MRI readout. In the current study, fMRI data was acquired using interleaved axial slice ordering. A slice at the top of the brain was acquired followed by consecutive even numbered slices (n=2, 4, 6,…). The interleaved acquisition then restarted with acquisition of odd-numbered slices (n=3, 5, 7,…). This process continued until signal from the whole brain is acquired. For our, high temporal resolution, 7 T fMRI acquisition, traditional slice timing correction was not applied. Instead we opted to apply the temporal derivative method[99] available in the FSL package. The temporal derivative method is a temporal filtering technique applied to acquisition slices. Recent studies have shown traditional slice timing

correction can be less effective in rsfMRI acquisitions with high temporal resolution (TR<3 seconds)[100], given that RSN's manifest in longer term signal fluctuations (0.01-0.1 Hz).

Temporal Filtering

The raw fMRI signal contains high frequency noise from cardiac pulsality, breathing, and other physiological processes. These high frequency noise components typically have temporal oscillation frequencies in the 0.3 – 1 Hz range[101]. Low frequency noise, in the range of 0 – 0.015 Hz, also affects the fMRI signal. Low frequency noise is generally attributed to scanner B_0 drift and head motion[102]. For the pre-processing applied to the fMRI time series data in our 7 T study, a high-pass filter was used to remove unwanted low frequency noise with oscillation frequencies below 0.01 Hz. A low-pass filter was not explicitly applied to remove high frequency noise due to risks of removing true RSN signal[103]. The rs-fMRI signal is generally in the 0.01 – 0.1 Hz range. However recent studies have shown higher frequencies associated with true neural firing also exist[104]. Instead of a low-pass filter, high frequency components were removed using spatial temporal ICA[101] (to be discussed shortly).

Spatial Smoothing

In fMRI data analysis, a Gaussian spatial smoothing kernel, is often applied to produce an image for which each pixel's intensity is the kernel-average of its neighbors. In BOLD fMRI, the extent of activation in both task-based and resting-state fMRI may be spatially

distributed. Consequently, spatial smoothing is applied to remove noise and isolate true, spatially consistent BOLD signal.

The extent of spatial smoothing may be quantified by the full width at half-maximum (FWHM) of a Gaussian blurring kernel. For our 7 T fMRI time series analysis, the width of the Gaussian spatial smoothing filter was set at 5 mm (for group level statistics). Our chosen FWHM (which is 2.5x the acquired voxel size) was conservatively estimated to minimize discrete random noise and facilitate region-of-interest analysis. The kernel size was also identified to account for individual subject variability in activation for end-stage, group-level analysis.

Noise Regression via Independent Component Analysis

Independent Component Analysis (ICA) was applied as a final, quantitative noise and artefact removal step. In FSL, ICA is implemented using the Multivariate Exploratory Linear Optimize Decomposition into Independent Components (MELODIC) tool[105]. MELODIC is a linear decomposition method that separates 4D fMRI time series data into spatio-temporal components[96]. Each resulting component corresponds to structured signal or noise.

The time series data for each subject enrolled in our study underwent ICA decomposition (producing 40-80 independent components). Components were manually classified as signal or noise based on spatial patterns of activation and component oscillation frequency. True resting state components exhibiting structured signal in gray with oscillation frequencies in the range of 0.01 – 0.1 Hz[101]. Noise components, including residual

physiological signal, motion artefacts, and MRI-system specific effects were removed. After manual classification of signal and noise, noise components were regressed from the raw input data. Some examples of signal and noise are given in the following figures.

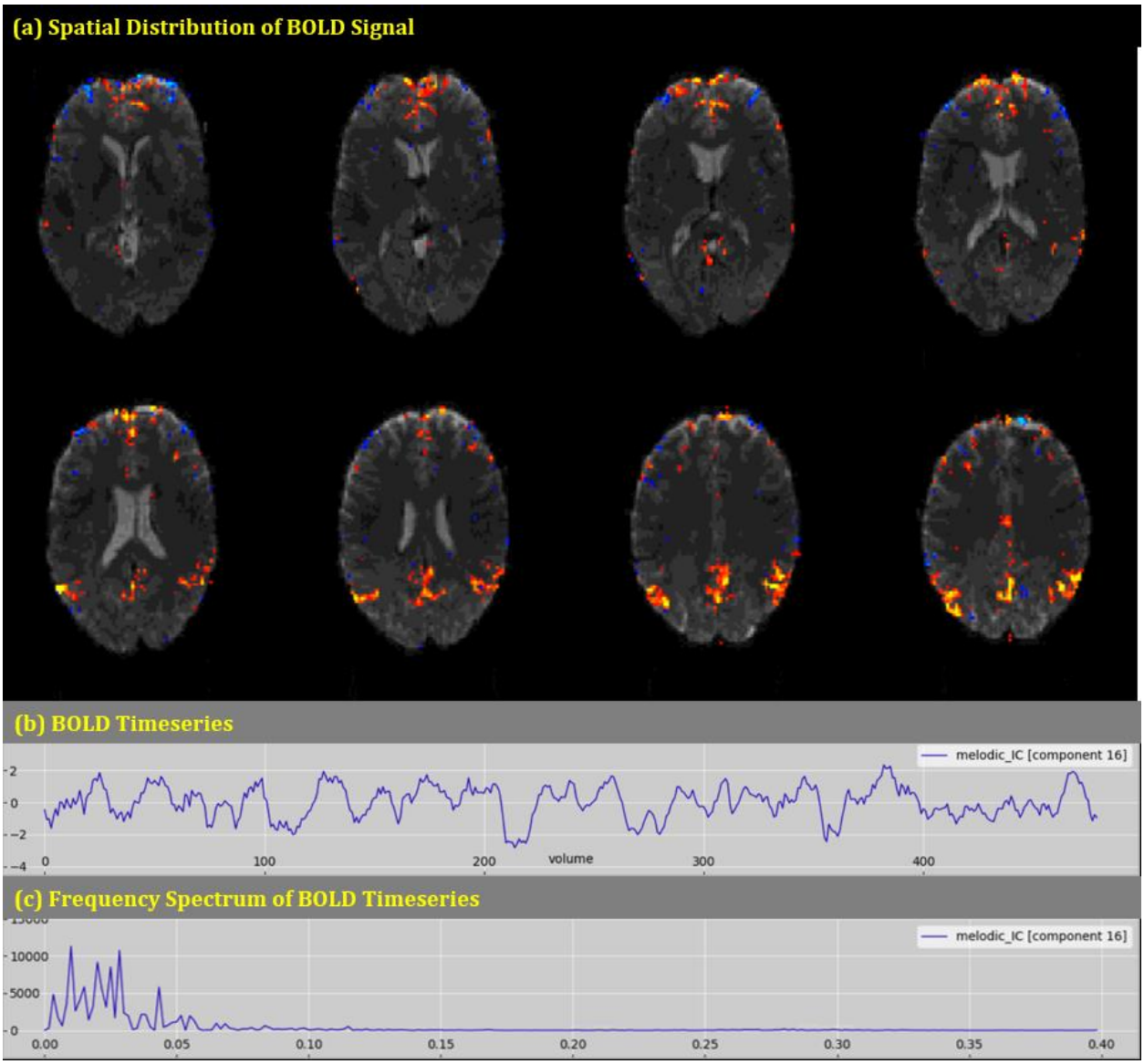

Figure 3.11: One component from an ICA decomposition that represents the DMN. The spatial distribution of BOLD signal is preferentially located in the posterior cingulate cortex and lateral occipital cortices, thresholded at Z=3. The timeseries shows relatively slow fluctuations and the frequency spectrum lies peaks in the 0.01-0.04 Hz range, within the 0.01-0.10 range that we expect to see RSN activity.

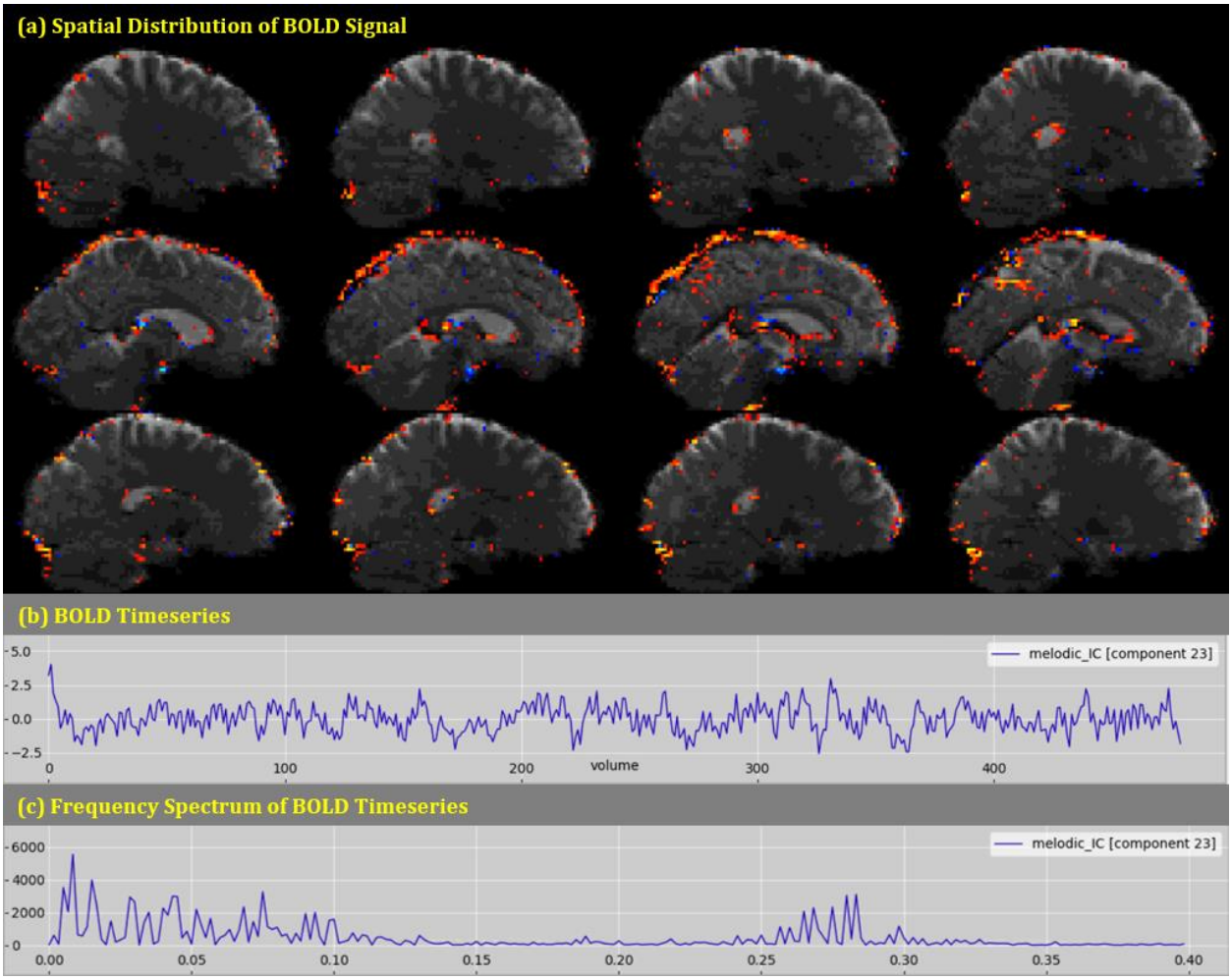

Figure 3.12: Artefactual venous circulation signal, characterized by strong BOLD activation in the sagittal sinus (Fig. 3.12a). The BOLD timeseries in Fig. 3.12b has a frequency spectrum (Fig. 3.12c) with peaks in the 0.01-0.1 Hz range. But a feature of the venous flow artifact is that it also shows power in the 0.25-0.3 Hz range. This differentiates artefactual venous signal from neural activity.

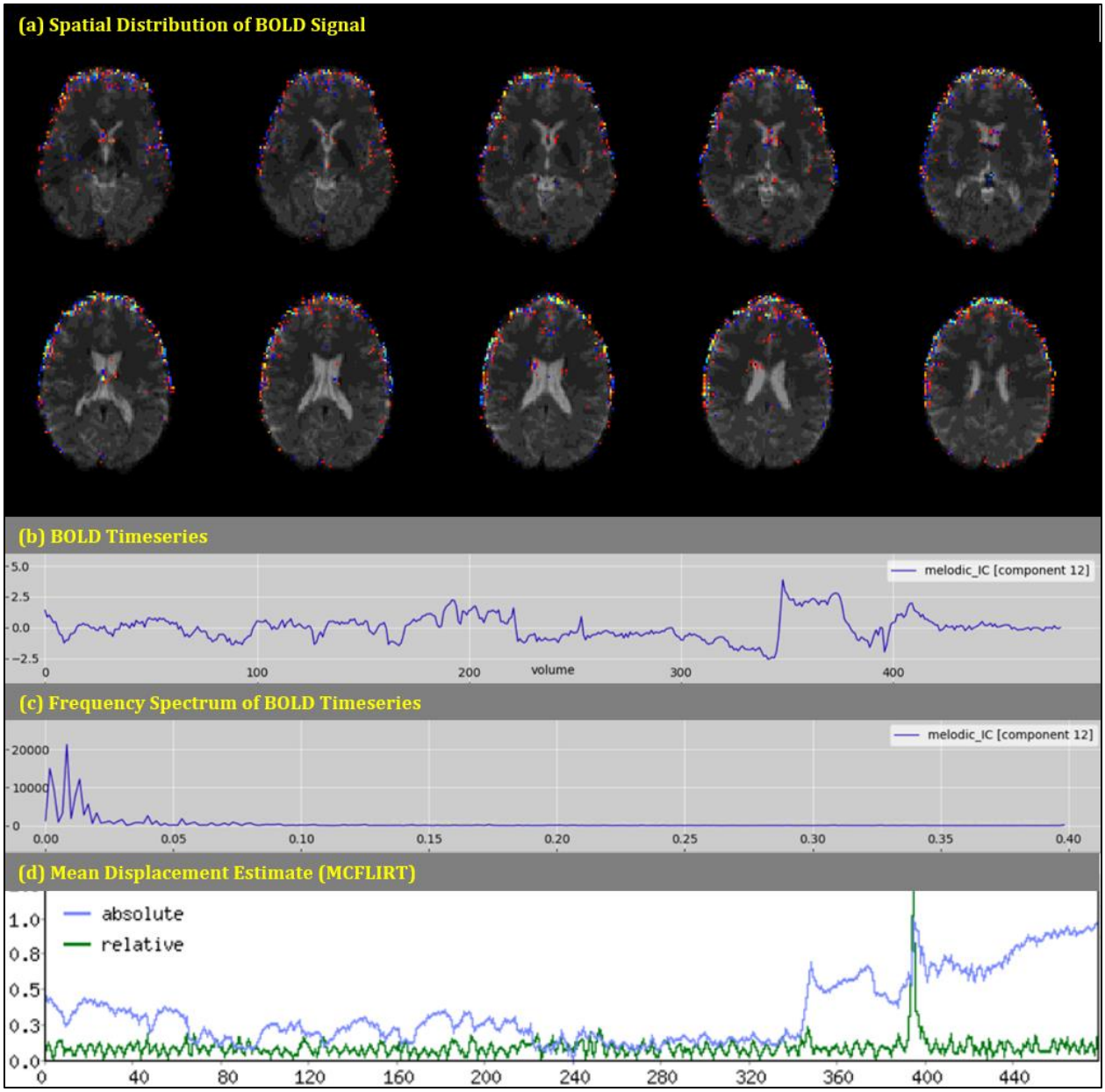

Figure 3.13: An ICA component representing head motion artifact. (a) The artefactual signal shows a characteristic ring structure around the brain. (b,c) Motion manifests as a spike in the BOLD timeseries. (d) Motion can also be identified based on the sharp increase in absolute displacement occurring at volume #350 in the Mean Displacement Estimate from MCFLIRT.

A Note on Global Signal Regresssion and Anti-Correlations

Anti-correlations in rs-fMRI data have particularly been observed when applying Global Signal Regression (GSR) for artifact removal[106]. GSR subtracts not only the mean CSF and WM time series signal, but also the average time series signal from all parenchymal brain tissue (including GM). Since BOLD signal and noise characteristics are different across control and patient groups, GSR may fail and introduce unwanted, spurious negative correlations[107]. Consequently, GSR was not applied in our study.

3.6 MRI Data Analysis

Three types of functional neuroimaging analysis were performed based on the pre-processed 7 T rs-fMRI data collected in our MS imaging study. First, dual regression[108], a fully data driven model, was used to calculate group-level ICA components and measure group differences between both MS phenotypes and controls within individual RSN's. Next, a set of 100 predefined regions of interest (ROI's) based on 14 known resting-state networks, compiled by the Stanford FIND Lab[109] were used in conjunction with the CONN toolbox[110] to evaluate both intra and inter-network connectivity measure. Finally, the regions of interest from the FIND Lab atlas were applied in a connectivity matrix apporoach for each subject. Connectivity matrices were evaluated using partial least squares (PLS) statistics[111]. PLS extracts the most probable functional connections contributing to group differences in connectivity and additionally tests for stability of ROI-to-ROI connectivities through boostrapping.

(i) Dual Regression

Dual regression requires prerequisite, group level spatial component maps, which represent RSN activation shared by all subjects. In our study, these maps were generated using group-ICA (GICA)[112]. GICA applies a temporal concatenation of all subject data followed by ICA decomposition to measure spatial components that are statistically independent and common across subjects. GICA-derived components represent (i) common shared RSN's and (ii) noise components. In the GICA implementation in FSL MELODIC[65] that was used in our study, initial data reduction occurred by projecting individual subject data

onto a common eigenbasis[113]. Components were then classified visually based on the spatial distribution of calculated components in the brain[101].

After the group template maps were identified from GICA, dual regression occurs in two multiple-regression steps.

First, a set of time courses are computed for each group map using the GICA spatial maps (independent variable) and each subject's timeseries data (dependent variable). The time courses describe the extent to which each component contributes to total BOLD signal. The time courses are then used in step 2, where they act as the model inputs (independent variable) for a second-stage regression against each subject's BOLD fMRI data (dependent variable). The result of the two-stage dual regression process is a set of spatial maps for each subject that reflect their extent of activation relative to the GICA component.

Based on the output of dual-regression, group-level differences were measured at the voxel using a general linear model (GLM). The GLM was built to establish group differences in functional connectivity between HC and RR subjects, HC and SP subjects, and RR and SP subjects. Sex, disease duration and Expanded Disability Status Scale were included as covariates in the GLM. All statistical tests were corrected for multiple comparisons using a family-wise error rate of $p < 0.05$.

(ii) Regional Connectivity Analysis (CONN Toolbox)

The CONN toolbox (version 17) was used to assess inter- and intra- RSN differences with 100 predefined ROIs from the Stanford FIND Lab Atlas[109], and ROIs were distributed among 10 known RSN's.

Regional connectivity was computed between all pairs of ROIs in the brain. Pairwise correlations were derived using Fisher Z-transformations of the BOLD time courses. Group-level differences in both inter- and intra- network FC strengths were then calculated employing two-sample t-tests. The results were corrected for multiple comparisons using non-parametric permutation testing[114]. Clusters of interest were identified based on a voxel-wise threshold of $p<0.01$. Each voxel within an ROI was tested for significance compared to the whole-brain activation probability density function using a permutation test with 1000 permutations. Significant connections were then determined by using a false-discovery rate threshold of $p<0.05$. Each ROI was characterized by its mass (sum of the F-statistics over all connections in each ROI), and the mass of reach ROI was compared to the distribution of expected cluster mass values under the null hypothesis, which was numerically estimated based on permutation testing with n=1000 permutations.

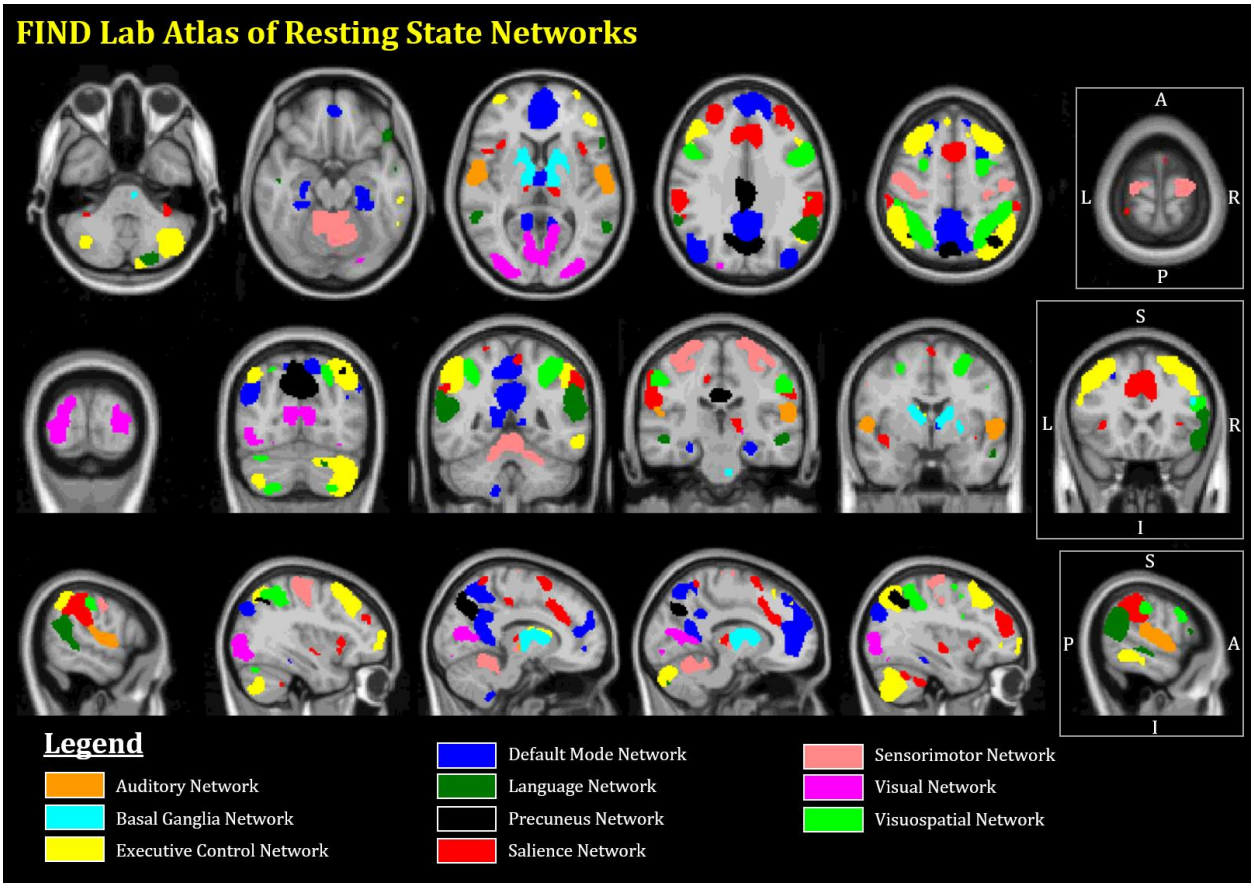

Figure 3.19: FIND Lab Resting State Network (RSN) atlas of the human brain. Resting state networks are labelled by color.

(iii) Correlation Matrix and Partial Least Squares Regression Analysis

Correlation Matrices

Correlation matrices were computed for each subjecting using the Stanford FIND Lab ROIs described in Section 3.6(ii). Specifically, for each subject, the average timeseries (after ICA de-noising) was computed within each ROI. This resulted in a 100 x 100 matrix of Pearson correlation coefficients. The connectivity matrix was organized such that the first 50 rows and columns represent left-hemisphere ROIs and the remaining 50 rows and columns represent the right-hemisphere. The entire matrix is symmetric about the diagonal

and includes both inter- and intra-hemispheric connection. Within the left and right hemispheres, ROIs were ordered such that the largest RSN's appeared first (closest to the top of the matrix). Average group-level matrices are shown in figure 4.7 of the results.

Partial Least Squares Regression

Partial least squares (PLS) regression[115] is a technique that has been applied in resting-state network modeling, to extract salient group differences in brain connectivity patterns. PLS is a statistical method designed to find weighted linear combinations of vectors that express maximum covariance between two or more ordered datasets. In this case, the data sets were rs-fMRI time series for each individual subject in our study. As input, PLS takes a correlation matrix (X) and a matrix of subject phenotypes (Y). In our study, X was represented as a 40x4950 matrix where each row contains correlation data from one subject. Y was a 40x3 matrix denoting HC, RR, and SP phenotypes.

The inter-relation between X and Y can then be summarized using the matrix equation M=X'Y. In PLS, M undergoes singular value decomposition into left and right singular value matrices, as well as a diagonal matrix of singular values:

$$M' = USV'$$

Where:

- U is the left singular matrix. U has a size of 4950x3 in our work.
- S is a diagonal matrix of singular values with size 3x3.

- V' is the right singular matrix with size 3x3.

Notably, the left and right singular matrices have the property $U^T U = I$ and $V^T V = I$, where I is the identity matrix.

A set of *latent variables (LV)* can be derived from U, S and V by taking values from the i^{th} column of U and V and the i^{th} diagonal element of S, forming a triplet for each LV set[115]. The number of LV sets is equal to the rank of matrix M, which was 3 in our study. Each LV set comprises (1) the correlation matrix that expresses group differences (U), (2) the relative size of the singular value (S), and (3) the correlation of each phenotype with the expressed correlation matrix of group differences (V).

To measure group connectivity differences with PLS, the latent variables are each tested for statistical significance using permutation methods[115]. 500 permutations are tested, each time generating a singular value. The p-value for significance is therefore equivalent to the fraction of singular values greater than that of the original, non-permuted matrix. For statistical significance, $p < 0.05$ (i.e. less than 25 of 500 permutations exceed the original SV).

PLS was also applied to find the most stable ROI-to-ROI connections via bootstrapping with replacement. Rows in the X and Y matrices (i.e. individual subject correlation matrices and phenotype) were randomly sampled with replacement, and the resulting matrix M underwent SVD to generate a new set of LV's. The weights of the new LV's, sampled 500 times, which generated a distribution of saliences for each ROI-to-ROI correlation. Each salience had an associated standard error. The singular value weight divided by the standard

error is the bootstrap ratio (BSR) for each ROI-to-ROI correlation. The BSR is approximately equal to the Z-score if the standard error distribution is approximately normal[115]. Therefore, the greatest contributions of interest at a 95% confidence can be obtained by thresholding the results to BSR>1.96. The thresholded BSR correlation matrix reveals the RSN's that contribute most to group differences in connectivity.

Finally, the left singular vector can be projected onto each individual subject's correlation matrix to compute a "brain score" for each individual[115]. Brain scores identify the quantitative contribution of each subject to the group differences in global connectivity patterns.

4. Results

4.1 Baseline Cognitive Testing and Structural Neuroimaging Characterization of our Cohort

Baseline cognitive tests were administered to measure memory, attention, executive function, and processing speed for all subjects included in our cohort. Structural image processing was performed based on the 0.7 mm^3 isotropic resolution T_1-weighted anatomical MP2RAGE data collected in our study. Regional and global brain volumes and cortical thickness were measured using FreeSurfer. Demographic, clinical, and cortical thickness characteristics of subjects enrolled in this study are summarized in table 4.1.

	HC (n = 15)	RRMS (n = 14)	SPMS (n = 11)
Male : Female Population	6M : 9F	5M : 9F	3M : 8F
Age	43.6(7.93)	43.4(6.80)	49.8(5.06)[b,c]
Education Level (Years)	16.13(2.42)	15(1.92)	13.82(1.60)[b]
EDSS Score		1.89 (1.33)	4.59 (1.69)[c]
Disease Duration (Months)		133.6 (76.0)	221.6 (94.0)[c]
Cortical Thickness (mm)	2.289 (0.1036)	2.200 (0.0971)[a]	2.167 (0.1459)[b]

Table 4.1: Demographic and clinical characteristics between cohorts. Statistically significant group differences are noted as follows:
[a] HC vs. RRMS: cortical thickness $p<0.030$.
[b] HC vs. SPMS: age $p<0.022$, education level $p<0.007$, cortical thickness $p<0.039$.
[c] SPMS vs. RRMS: age $p<0.013$, disease duration $p<0.022$, EDSS $p<0.0003$.

Neuropsychological test results are summarized in the following box-and-whisker plots, highlighting statistically significant differences at $p<0.05$. A numerical summary of figures is also found in Appendix A.1-A.3.

Overall, RRMS patients showed statistically significant decreases in cortical thickness compared to HC ($p<0.03$), and no differences in neuropsychological testing.

SPMS patients had lower education levels compared to HC ($p<0.007$), and in neuropsychological testing, worse scores on SDMT ($p<0.009$), WAIS-III ($p<0.001$), PASAT-3 ($p<0.03$), higher levels of fatigue (MFIS) ($p<0.00001$), and higher levels of depression (BDI-II) ($p<0.013$).

Finally, comparison of SPMS with RRMS reveals the former is older on average ($p<0.013$) and have lived with the disease longer ($p<0.0003$). In neuropsychological testing, SPMS subjects showed higher fatigue (MFIS) ($p<0.04$).

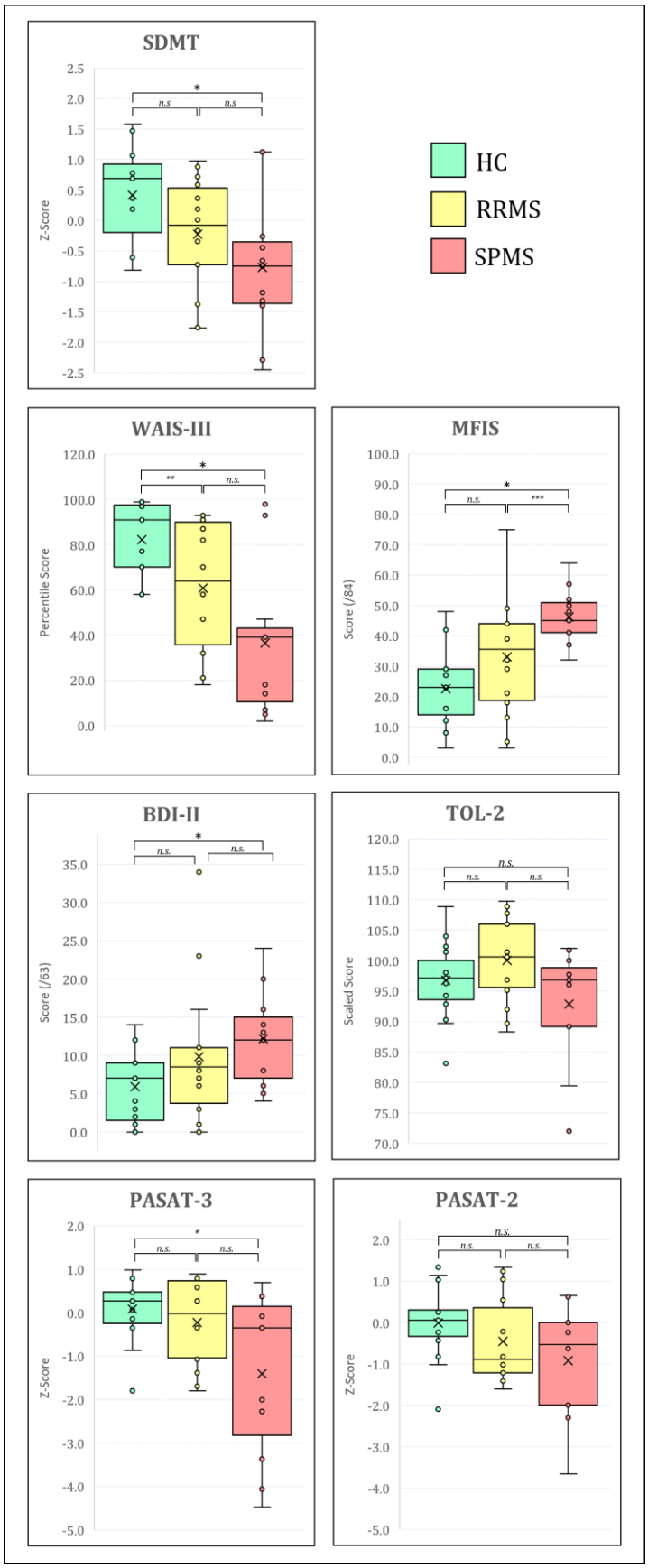

Figure 4.1: Neuropsychological test score results for HC, RRMS and SPMS subjects. Statistically significant differences are noted as follows:
* HC vs. SPMS: SDMT p<0.0094, WAIS-III p<0.001, MFIS p<0.00001, BDI-II p<0.013, PASAT-3 p<0.03
** HC vs. RRMS: no statistically significant differences
***RRMS vs. SPMS: MFIS p<0.039

4.2 Dual Regression

The group ICA (GICA) decomposition of denoised resting state timescourses from our study yielded 20 independent components. Eight of the components were manually identified to be true resting state networks[116]. Figure 4.2 below shows GICA-derived common resting state networks shared between HC, RR and SP subjects:

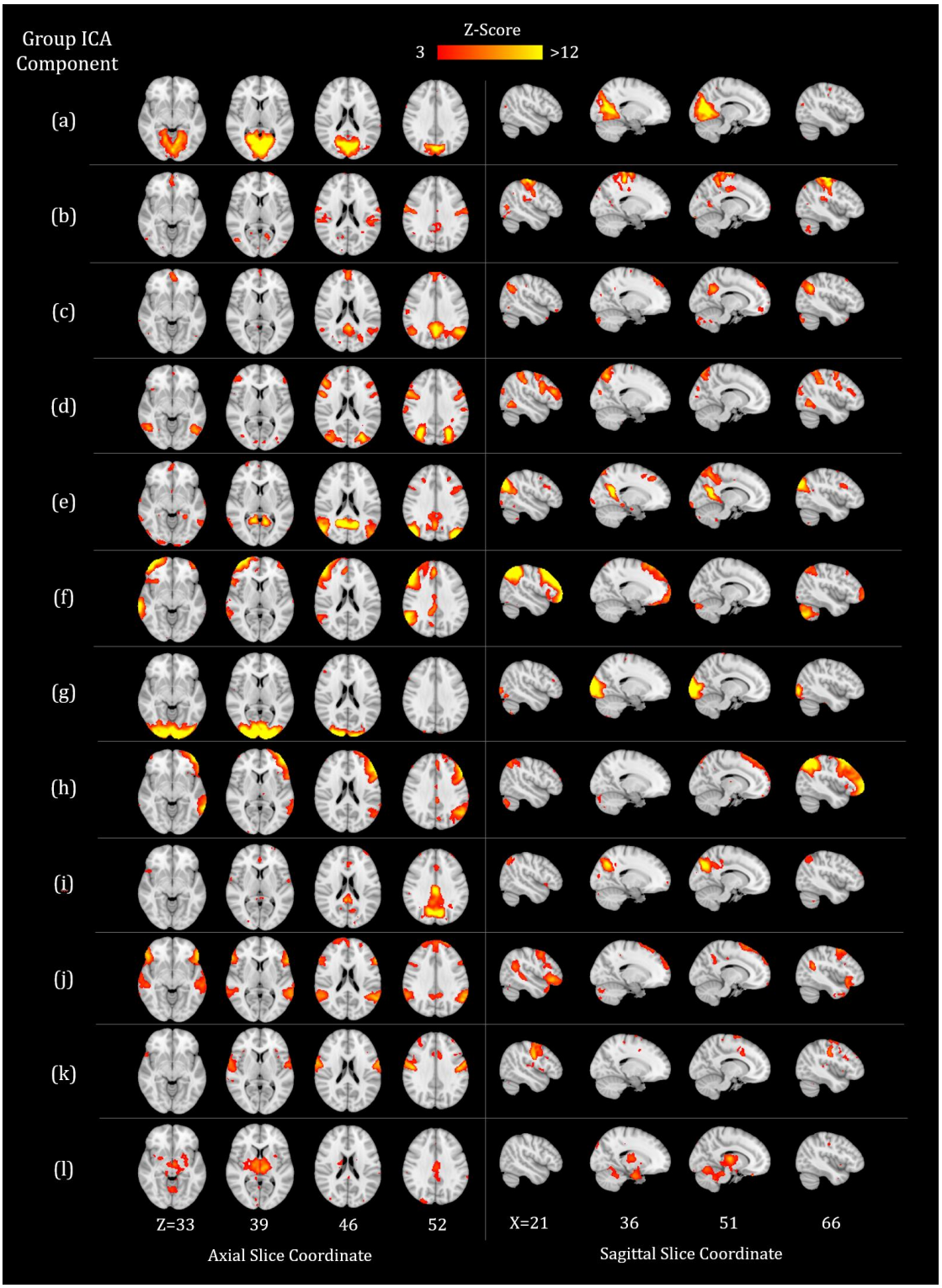

Figure 4.2: Axial and sagittal views of twelve RSNs derived from gICA in our population of HC and MS subjects. Coordinates are based on the MNI152 2mm atlas space and thresholded at the level Z=3. From top to bottom, RSNs correspond to: (a) visual, (b) sensorimotor, (c) dorsal DMN, (d) visuospatial, (e) ventral DMN, (f) right ECN, (g) high visual, (h) left ECN, (i) precuneus, (j) language, (k) auditory, (l) basal ganglia/precuneus.

These networks were highly robust, exhibiting strong activation patterns that were spatially consistent with previously recognized resting-state activation patterns observed in large cohort studies[109].

Dual regression was applied to the GICA-derived components to evaluate group differences in activation between Healthy Control (HC), Relapsing Remitting (RR), and Secondary Progressive (SP) MS subjects. Statistical inference was specifically carried out using a GLM design. Two statistically significant findings were seen in RRMS patients compared to HC.

In the primary visual RSN, which is associated with information processing of stationary and moving objects[117], RRMS subjects displayed increased activation in the precuneus cortex, calcarine cortex, and lingual gyrus. In the sensorimotor network, which is associated with planning and execution of motor tasks, RRMS subjects showed greater activation in the pre- and post- central gyri and the posterior cingulate gyrus. Results were reported with a significance threshold of $p<0.05$, corrected for multiple comparisons. No significant effects were found when comparing resting state activation of SPMS subjects to HC and RR.

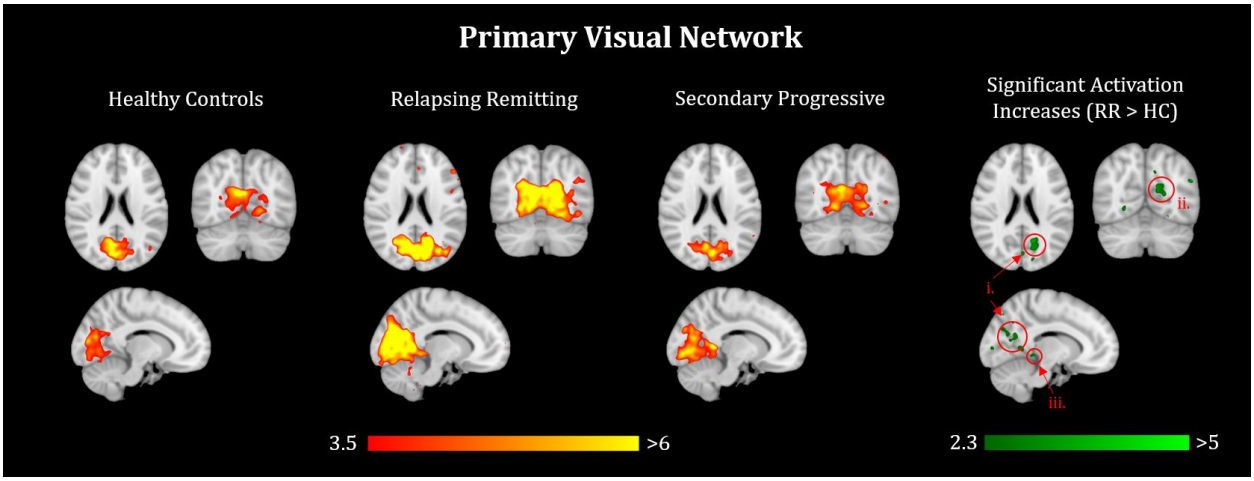

Figure 4.3: Group expression of the primary visual network for HC, RRMS, and SPMS is displayed in columns 1-3, respectively, representing average expression of the RSN for members of the cohort. Statistically significant increases in RRMS activation compared to HC are highlighted in column 4. Key areas are (i) precuneus cortex and (ii) calcarine cortex, and (iii) lingual gyrus regions. Results were corrected for multiple comparisons and are reported with a threshold level of $p<0.05$.

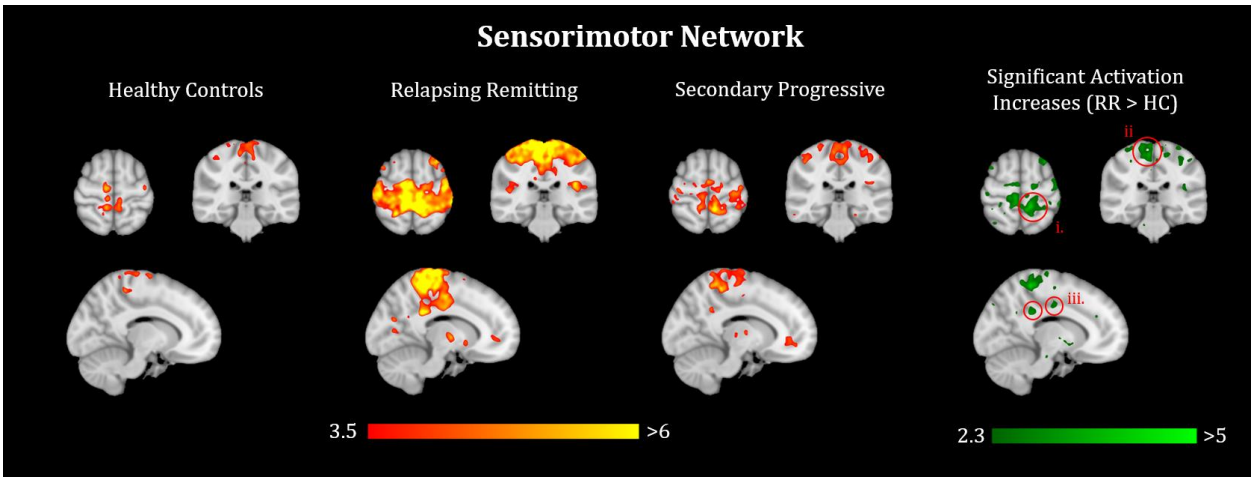

Figure 4.4: Group expression of the sensorimotor network for HC, RRMS, and SPMS is displayed in columns 1-3, respectively, representing average expression of the RSN for members of the cohort. Statistically significant increases in RRMS activation compared to HC are highlighted in column 4. Key areas are (i), (ii) pre- and post-central gyri, and (iii) the posterior division of the cingulate gyrus. Results were corrected for multiple comparisons and are reported with a threshold level of $p<0.05$.

4.3 Inter-Regional Connectivity Alterations in MS Evaluated using CONN Toolbox

Several connectivity alterations were revealed by regional connectivity analysis within the DMN. RRMS subjects, compared to HC, had decreased connectivity between the thalamus and the posterior cingulate cortex (PCC) and the superior lateral occipital cortex (OCC-ls) ($p<0.005$). By contrast, connections between the parahippocampal gyrus (PHG-pd) and the left and right precuneus cortices (PCUN-L and PCUN-R) and the PCC were strengthened ($p<0.008$) , as well as the PCC-PCUN-R connection ($p<0.005$).

SDMT scores, measuring cognitive processing speed, were strongly correlated with the strength of thalamic connections with the PCUN-L/PCUN-R, left and right hippocampi (HPC), PHG-pd, and the frontal pole ($p<0.03$).

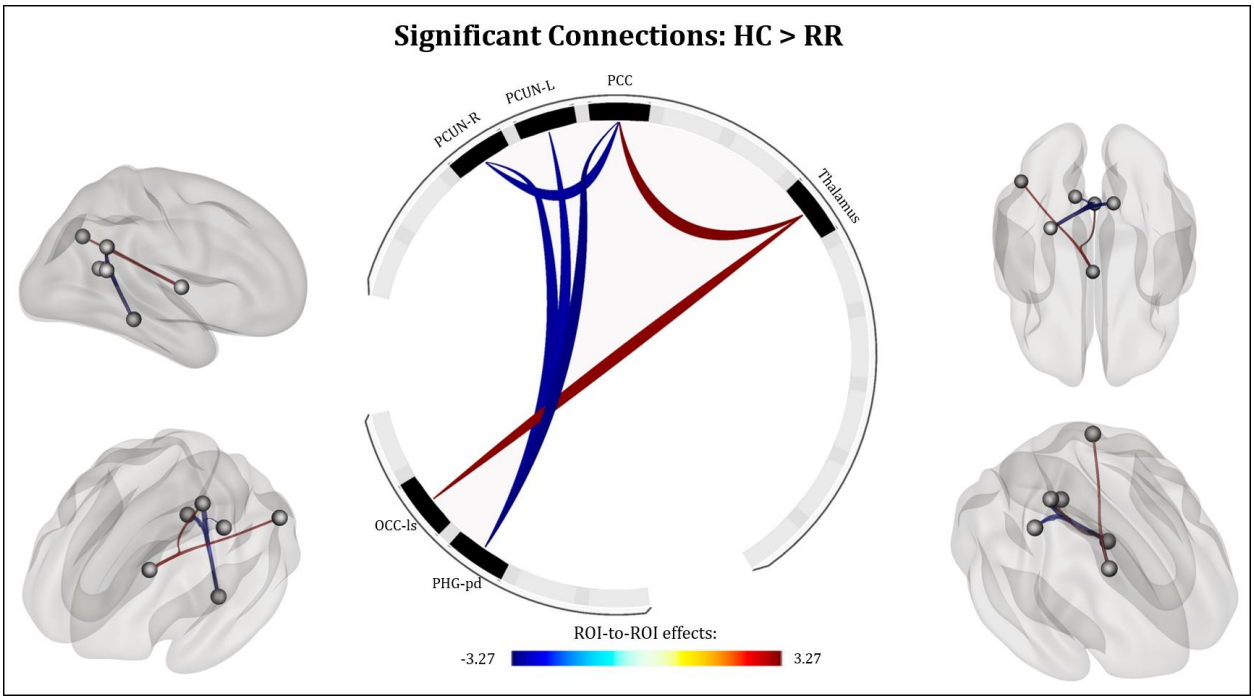

Figure 4.5: Significant FC differences between healthy controls and RRMS subjects within DMN ROI's. Healthy controls showed stronger thalamus-PCC and thalamus OCC-ls connectivity compared to RRMS subjects (red connections) ($p<0.005$). RRMS subjects had increased connectivity compared to HC in the PCC-PCUN-R ($p<0.005$), PHG-pd-PCUN-R, PHG-pd-PCUN-L and PHG-pd-PCC connections ($p<0.005$) (blue connections).

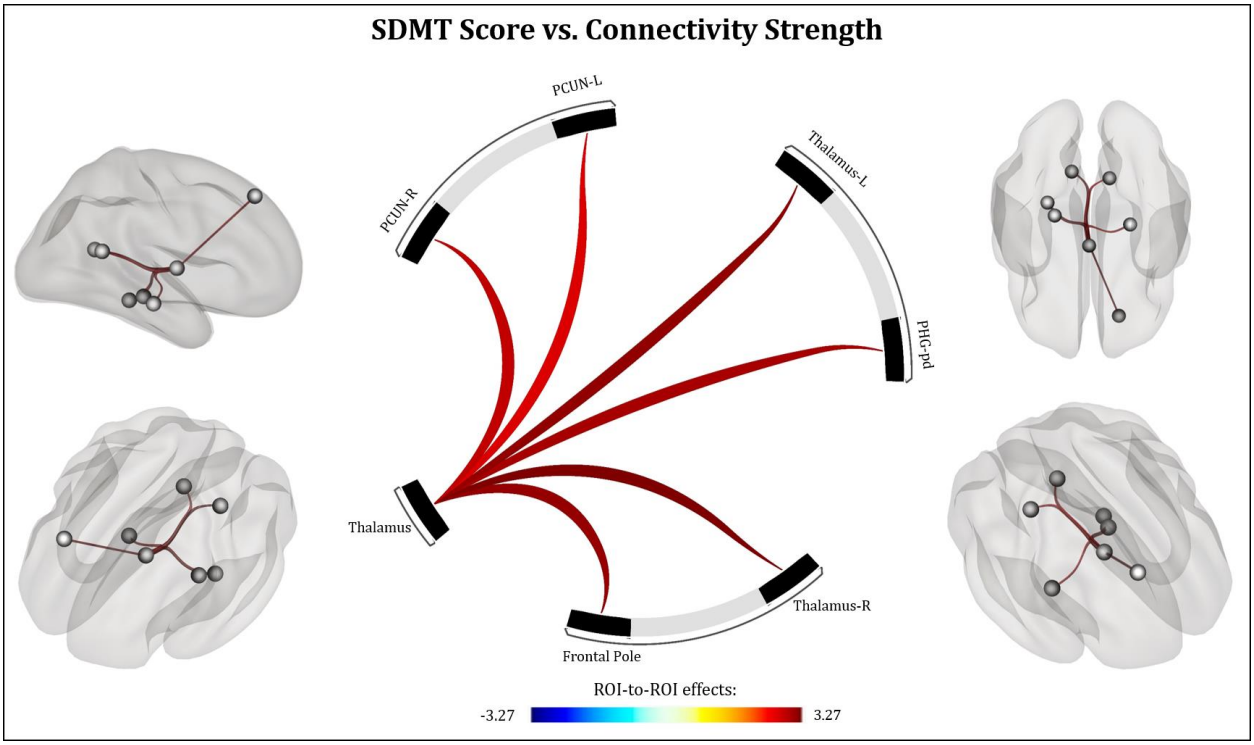

Figure 4.6: Significant FC correlations between SDMT and thalamic DMN ROI connectivity. Higher SDMT scores were correlated with increased connectivity between the thalamus and other regions (PCUN-L, PCUN-R, HPC-L, HPC-R, PHG-pd, and frontal pole) of the DMN ($p<0.03$).

4.4 Correlation Matrix and Partial Least Squares Evaluation

Using 100 ROIs derived from the FIND Lab atlas (reference), individual resting-state correlation matrices are plotted. Visualization of average group matrices are shown in figure 4.7 below.

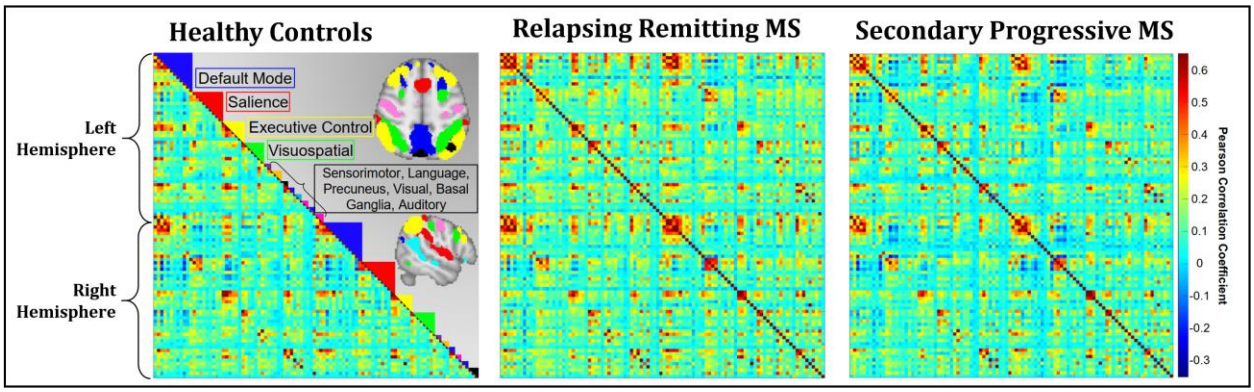

Figure 4.7: Average functional correlation matrices for HC, RRMS and SPMS groups. Individual resting state networks are denoted on the diagonal. Color schemes are consistent with Figure 3.19 for visualization purposes.

Partial least squares regression was applied to the group correlation matrix constructed from all subjects to yield a set of Latent Variables (LVs). The LVs can be used to evaluate group connectivity differences between HC, RRMS, and SPMS subjects. The LVs were specifically extracted in the order to quantify of the amount of covariance between rsfMRI signal and subject group (HC, RR or SP). RRMS subjects showed higher expression of the ROI-to-ROI connections highlighted by the thresholded bootstrap ratio (BSR) matrix in Figure 4.8. The BSR matrix depicts connections which contribute most to group-wise differences in resting state connectivity. Many connections lie in the Default Mode Network (DMN) and Executive Control Network (ECN).

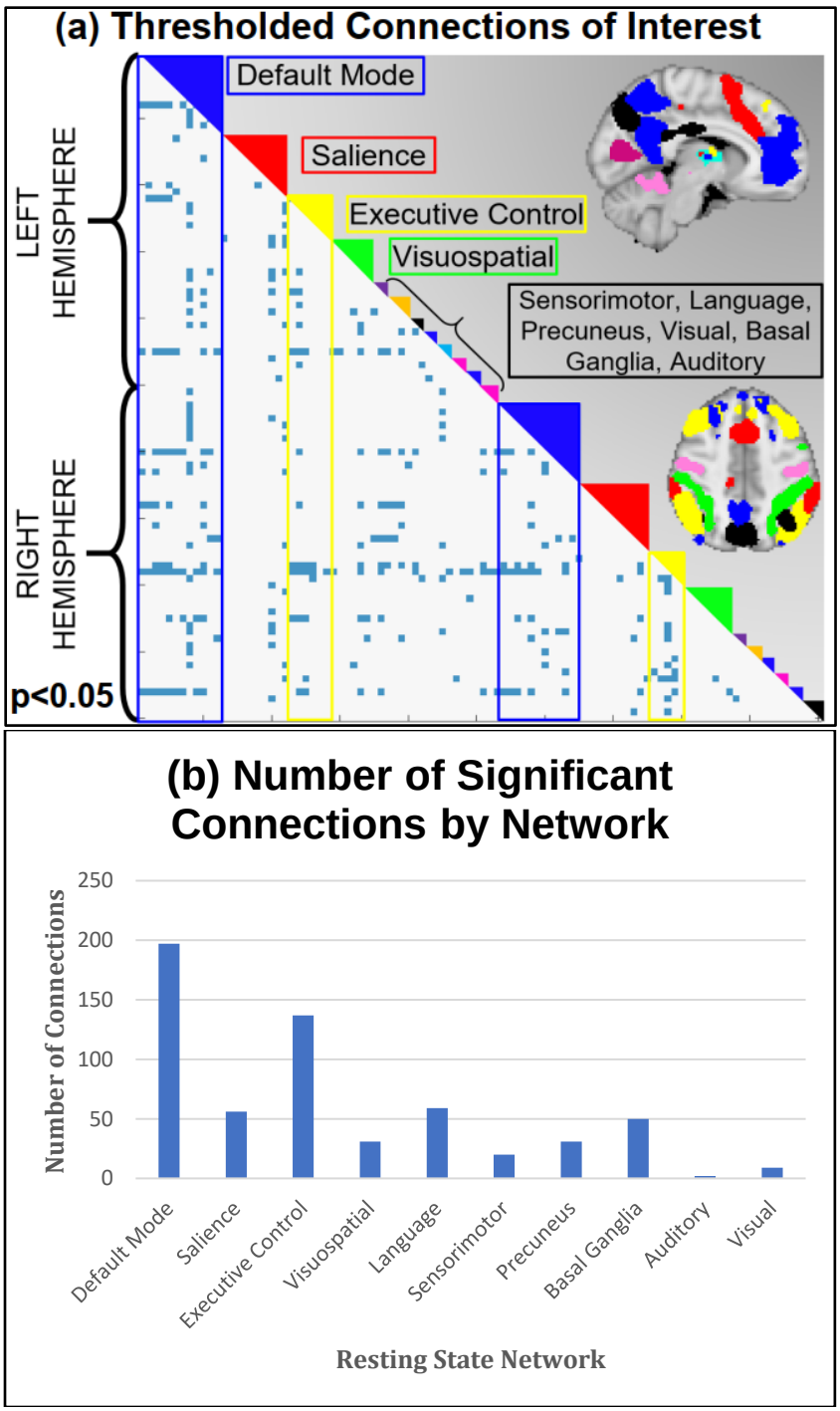

Figure 4.8: Thresholded Bootstrap Ratio (BSR) matrix showing ROI-to-ROI connections that contribute most to group-wise differences. The majority of the significant connections are within the default mode network (blue) and the executive control network (yellow).

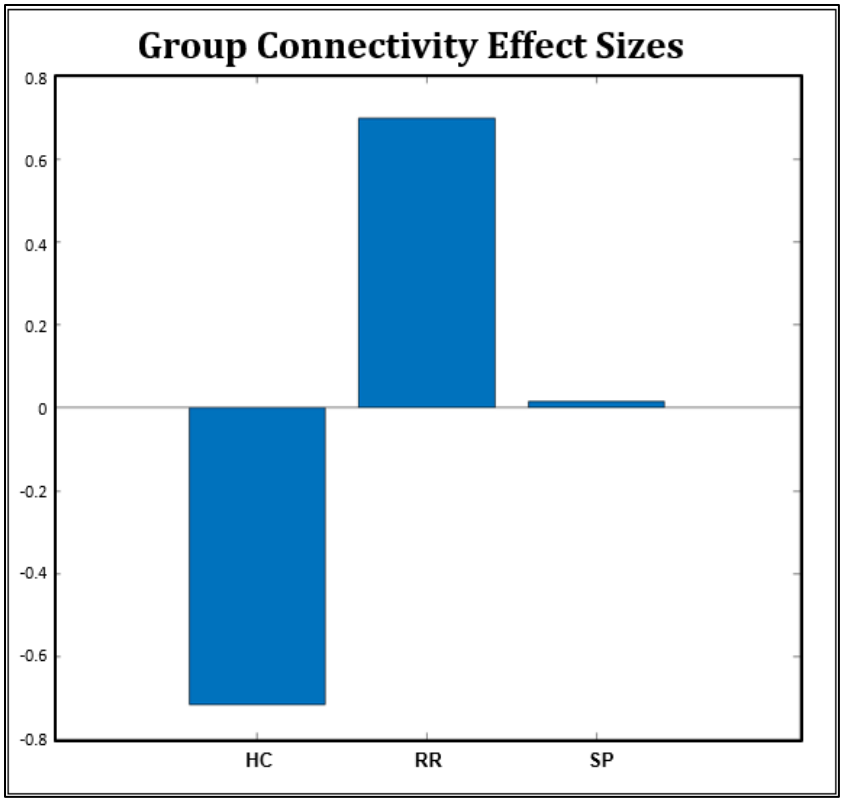

Figure 4.9: Total effect size derived from the BSR matrix significant connections (fig 4.8). A positive value for RRMS subjects suggests stronger expression of the BSR matrix compared to HC and SPMS.

A brain score for each subject was derived from the singular value decomposition of the connectivity matrices. The brain score identifies the quantitative contribution of each subject to the group differences in global connectivity. Brain scores from PLS (fig. 4.10) regression identified increased global connectivity in RRMS. More specifically, there were statistically significant increases in brain score of RRMS subjects compared to HC ($p<0.0006$). There were also significant increases in brain scores of SPMS subjects compared to HC ($p<0.002$). No brain scores differences were observed between RRMS and SPMS subjects ($p<0.075$).

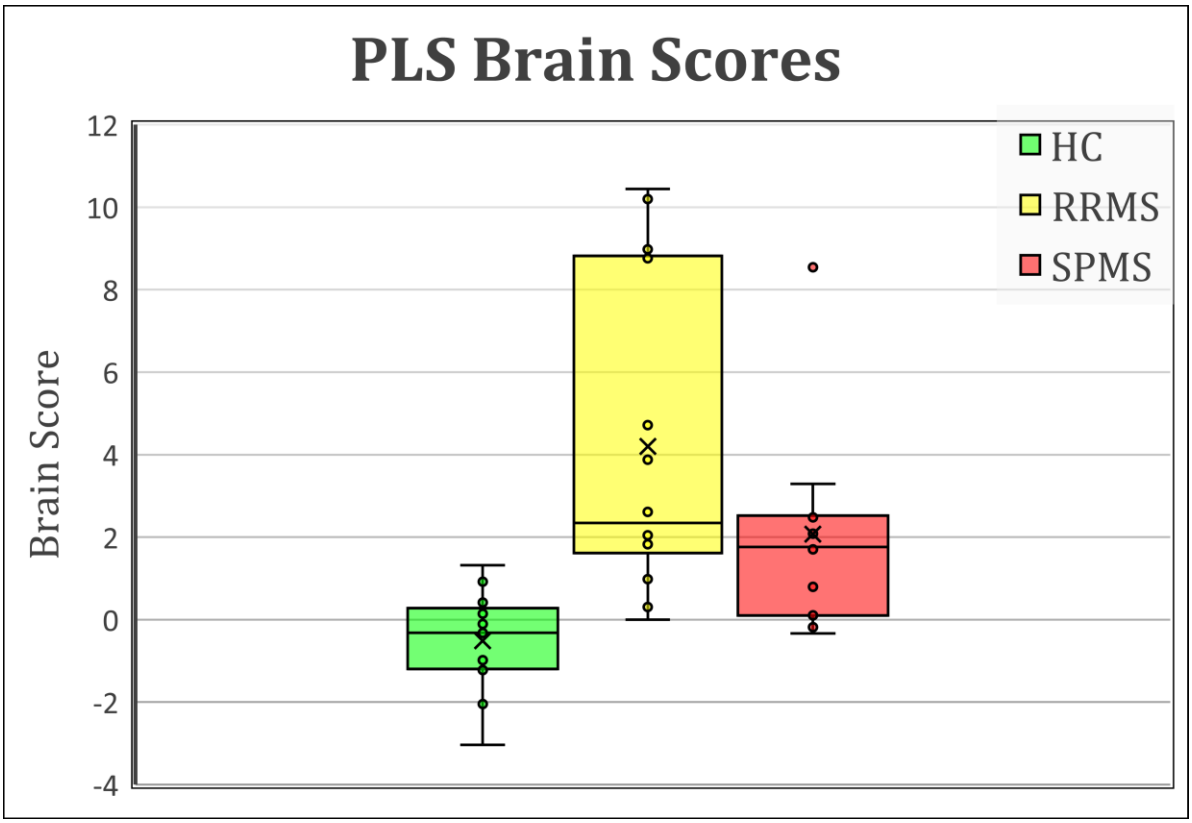

Figure 4.10: Brain scores derived from PLS. RRMS brain scores were highest, on average, and greater than HC ($p<0.0006$).

4.5 Relating Brain Scores to Cognitive Metrics

PLS brain scores were related to neuropsychological testing results using simple linear regression. The goal of this analysis was to assess the relationship between whole brain connectivity patterns and cognition in the MS and HC group. Using bootstrap resampling (5000 bootstrap re-samples) we estimated the 95% confidence interval for a linear regression relating brain scores to the cognitive testing data collected in our study. A subtle relationship was observed between PLS brain score and both PASAT-2 and PASAT-3 scores in HC. PASAT-2 and PASAT-3 differ based on the time given between each stimulus (2 seconds vs. 3 seconds) during the neuropsychological test. A weak positive correlation

between PASAT2 test performance and PLS-derived brain score was found for HC subjects (R^2 = 0. 32). A similar weak correlation between and PLS-derived brain score was also found (R^2 = 0. 15).

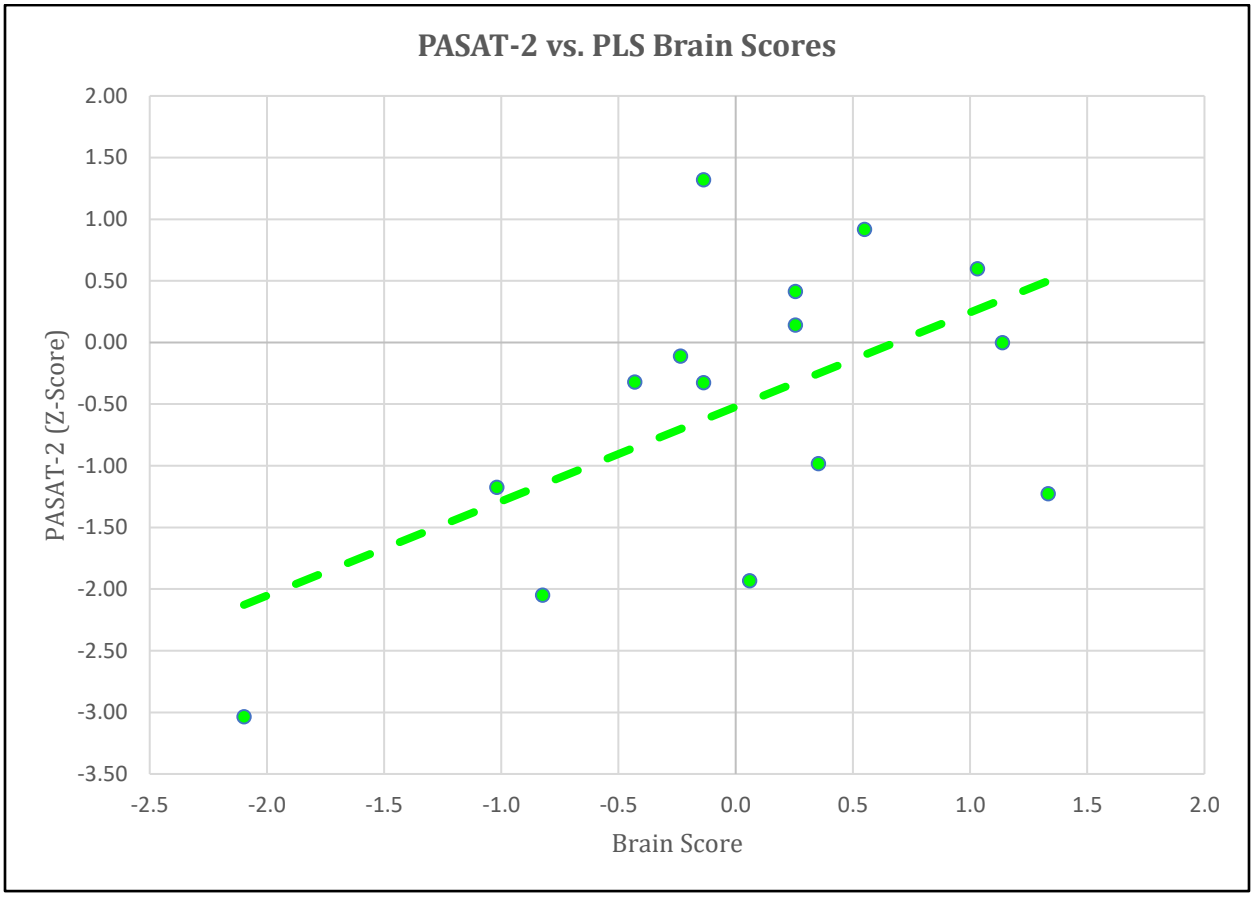

Figure 4.11: PASAT-2 Z-scores plotted as a function of PLS-derived Brain Scores (R^2=0.32).

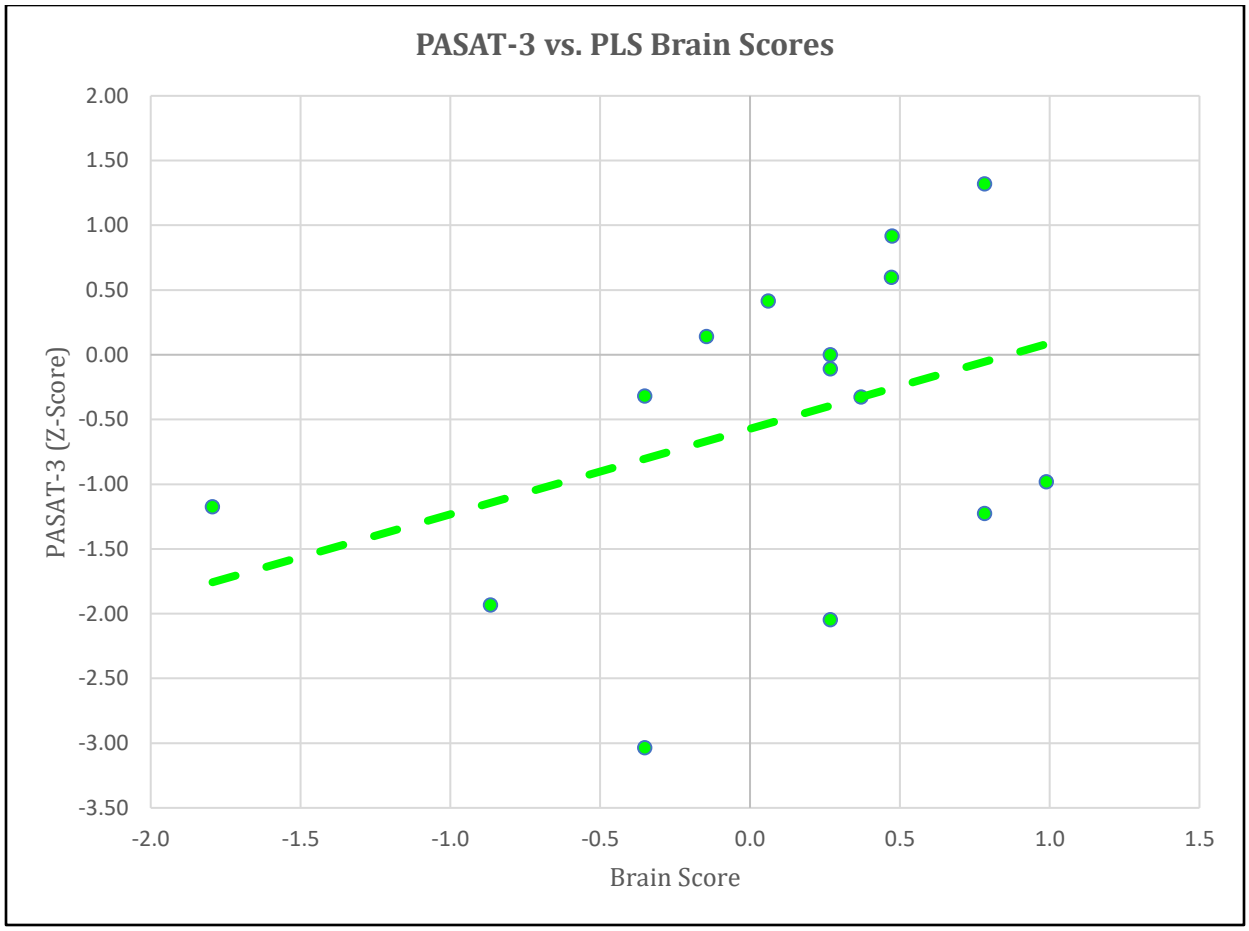

Figure 4.12: PASAT-3 Z-scores plotted as a function of PLS-derived Brain Scores (R^2=0.1535).

5. Discussion

In this thesis, resting-state functional connectivity of two cohorts of multiple sclerosis patients and one group of age, education and gender-matched healthy controls was studied using three different neuroimaging statistical analysis pipelines. An overall goal was to uncover group differences in 7 T resting state BOLD activation indicative of demyelination, axonal loss or adaptive network changes in response to neuroinflammation.

All network evaluation began with a pre-processing pipeline to correct for imaging artefacts, machine noise, and physiological noise. For 7 T resting state fMRI studies, the nature of the selected pre-processing is vital[118]. For the MS patients enrolled in our study, scanned using a 7 T head-only MRI scanner, we observed patient head motion could significantly impact individual and group ICA results. For this reason, careful denoising was applied at the single subject level to all timeseries data we collected. Careful attention was also paid to artefactual cardiac signals (both first and higher harmonics) that spatially resembled true resting state BOLD activation.

Consistent pre-processing was applied, irrespective of the end-stage statistical inference method used for whole-brain and local connectivity evaluation. Specifically, motion outliers were removed if volume-to-volume displacements exceeded 0.9mm, high-pass filtering was consistently applied with a cutoff of 0.01 Hz, and spatial smoothing was performed using a 5 mm FWHM kernel. ICA decomposition separated the total signal into independent components, representing either true resting state BOLD signal or noise. Manually classified noise was then regressed from the resting state time course to generate

an effective data set for analysis in group ICA and dual regression, and ROI-to-ROI analysis in CONN toolbox and PLS statistics.

Dual regression and corresponding GLM analysis showed the RRMS subject group in our study had higher activation compared to HC in the precuneus cortex, calcarine cortex, and the lingual gyrus of the primary visual network. The increase in visual network activation was one of the earliest results from fMRI, where studies of MS patients with a particular condition called optic neuritis showed similar increased activation in the calcarine sulcus[56]. In general, greater activation in a brain region may superficially be a favorable trait for neurological function, however a growing body of research suggests that these increases may be an unsustainable short-term compensatory mechanism to address structural axonal damage, leading to detrimental long-term effects on brain function[35]. More severe tissue damage is typical for later stage SPMS subjects[74], and is also reflected in the systemically decreasing brain scores derived from PLS.

The second finding from dual regression was in the sensorimotor network, where RRMS subjects showed increased activation in the pre- and post-central gyri and posterior cingulate gyrus compared to HC. This results corroborates a previous finding by Faivre et al.[119], whose group demonstrated sensorimotor network activation increases in RRMS at 3 T. Furthermore, task-based fMRI experiments have shown increased postcentral gyrus activation during passive hand movement[120] and repetitive thumb flexion[121]. The ground truth may be more nuanced, as other studies have found decreased left-right pre-central gyri connectivity in RRMS[6872], highlighting that the sensorimotor network as a whole may be rearranging. Typically, the precentral gyrus is associated with voluntary movement, and the postcentral gyrus with proprioception. In the bigger picture, we may be seeing short term

compensatory BOLD signal increases associated with proprioceptive function in RRMS patients as a manifestation of local network adaptations. Later stage MS may render these mechanisms insufficient, leading to proprioceptive and motor dysfunction characteristic of progressive MS.

Regional connectivity analysis revealed several alterations in DMN connectivity. The DMN is functionally involved in self-awareness, reasoning and episodic memory[32], and includes the thalamus, PCC, medial prefrontal cortex, and angular gyri. Disruptions in DMN connectivity are a known phenomena in MS[64,65] and other neurological conditions[32]. Comparison of RRMS with HC revealed both increases and decreases in DMN connections. Namely, lower FC was observed in thalamic-PCC and thalamic-OCC connections, which notably correlates to thalamic atrophy, a well known correlate of MS disease progression[122,123]. Furthermore, our cohorts showed clear decreases in average cortical thickness globally in RRMS and SPMS subjects compared to HC. In contrast, stronger FC was seen in other connections of the DMN, name the PHG-PCUN, PHG-PCC, and PCC-PCUN. It is worthwhile to note the posterior localization of these regions, and most notably the PCC which is a central node of the DMN[124]. Bonavita et al.[65] have also reported similar increased FC in short range PCC-focused connections of RRMS subjects, accompanied by disrupted longer range connections and gray matter atrophy.

The second notable finding in regional connectivity analysis was a direct correlation between thalamic connectivity in the DMN and cognitive processing speed, measured via SDMT cognitive testing scores. Several groups have previously identified the relationship between thalamic connectivity and cognitive performance in RRMS[125,126]. However, our work was a more general result that correlated all subjects' SDMT scores with thalamic FC.

A statistically significant result was not achieved in separate analysis of groups, which is likely a consequence of sample sizes (see section 5.1: Limitations and Future Direction).

With PLS analysis, correlation matrices were first computed for each subject based on predefined ROI's of 10 known RSN's. SVD of resulting correlation matrices generated statistically significant LV sets that revealed global increases in RRMS connectivity. The effect was largely contributed by connections within and between the DMN and ECN. Each individual subject's expression of the BSR matrix was quantified by the brain score. The brain score was a projection of the left singular vector of the group correlation matrix onto each individual's correlation matrix. The ECN is associated with many executive functions including working memory, attention, and planning[127], and comprises anatomical regions including the dorsolateral prefrontal cortex, anterior cingulate cortex, bilateral angular gyri and bilateral angular gyri—almost all of which lie adjacent to DMN regions. The role of inter-network connectivity between default mode network and executive control has been touched on by Rocca et al.[128] who found decreased DMN-ECN in RRMS compared to controls. This difference is possibly explained by methodological differences in RSN network selection where the authors used an ICA approach to generate group level networks, as we did in dual regression. The ICA approach takes the whole study population into account, meaning that an overweighting of MS subjects will necessarily bias RSN's in that direction, as opposed to our predefined ROI's used in PLS statistics which eliminate the bias but at the cost of losing potential population-specific effects that may be present[118].

Another hypothesis to explain DMN-ECN interactions, given the physical proximity of their associated brain regions, may come from the "mixed rewiring effect", a phenomena first observed in schizophrenia patients[129]. In their 2015 study, Littow et al. observed spatial

shifting and mixed functional signal patterns between regions of the very same networks, the DMN and ECN. If applicable to our MS cohorts, it may explain our DMN-ECN interactions derived from PLS.

Finally, A positive relationship between brain score and both PASAT-2 and PASAT-3 scores was observed for healthy control subjects. This finding suggests that reduced activation in the DMN and ECN may be correlated with increased scores in PASAT. A more detailed examination of specific connections could be undertaken. As discussed in section 2.2, both increases and decreases between regions of the DMN manifest in MS, and it would be informative to understand how they translate to HC's. No relationships between the brain scores of MS patients and any of the cognitive variables were identified. However, standardizing the preprocessing pipeline and increasing subject recruitment would help establish more confidence in this result, or lack thereof.

The combined results of the three analysis methods evaluated in this thesis complement one another and help build a more complete picture of the FC changes occurring in MS. Broadly, we observed a global increase in resting-state FC of RRMS subjects compared to HC from PLS. The result contrasts local connectivity alterations, where we observed increased FC in the visual and sensorimotor networks (from dual regression) and both increases and decreases in the DMN, as well as correlations with cognitive processing speed (revealed by regional connectivity analysis). Degradation of thalamic connectivity with progression of disease from RRMS to SPMS is consistent with existing neuroimaging studies that have identified the thalamus as an early site of neurodegeneration and demyelination in MS[130]. Network topology in MS brain may exhibit adaptive changes in response to structural damage due to lesions, inflammation and axonal loss.

5.1 Limitations and Future Directions

There are a few limitations of the current study. The total sample size, 40 subjects divided into 15 HC, 14 RR, and 11 SP groups, is reasonably small. Our ongoing study is seeking to recruit additional subjects, and this may be beneficial to remove bias in group ICA network calculation. Also, the GICA-derived networks in the current study were derived from a subject pool comprising roughly 2/3 MS patients. This means the GICA components are partially biased towards an MS phenotype. Deriving unbiased GICA networks in the case of neurological disease imaging studies is an unsolved problem. The group resting state networks we derived are representations of the global MS and HC populations and, importantly, appropriately model noise that is typical of our 7 T rsfMRI. An alternative approach could be to use either pre-existing template maps from an atlas or to compute GICA maps from a completely independent rs-fMRI dataset which includes MS patients and matched healthy controls.

Another possible future optimization in the preprocessing pipeline could be to use automated methods for ICA denoising. Algorithms such as FSL's FMRIB's ICA-based Xnoiseifier (FIX)[131] can automatically classify noise after training. The Automatic Removal of Motion Artifacts (AROMA) tool[132] (which does not require training) has also been designed specifically for advanced motion artifact detection of ICA components.

In our PLS study, we believe a possible limitation was the available sample size. Motion artifacts and physiological signal, if not properly accounted-for, can cause spurious correlations in group PLS analysis. These effects could potentially be minimized in a larger

cohort study. PLS brain scores derived from rs-fMRI data did not show an association with neuropsychological testing. This may reflect our chosen PLS data processing strategy or a fundamental absence of correspondence between scores relating global brain activity to certain neuropsychological testing data.

Several possible future extensions of the current statistical neuroimaging analysis of MS brain connectivity exist. First, diffusion Tensor Imaging (DTI) data, which was acquired independently for each subject in our study with 3 T MRI, could be used to derive structural connectivity (SC) matrices based on number of tractography streamlines. Like FC matrices, structural connectivity (SC) matrices can decomposed using PLS regression. FC and SC can also be integrated to study the structure-function relationships[133].

A 24-month follow-up scan and cognitive testing was also carried out for each subject in our study. Future integration of follow-up scan data could allow analysis of longitudinal FC changes specific to RRMS and SPMS.

6. Conclusion

The present study used advanced 7 T fMRI methods to identify alterations in resting-state FC of RRMS and SPMS compared to controls. Both within and between network FC were evaluated in key brain networks. Dual regression analysis revealed increased activation in the visual and sensorimotor networks of RRMS subjects compared to healthy controls. This feature may be associated with local adaptive network alterations in RRMS.

Regional connectivity analysis using predefined ROI's revealed increased FC in short-range posterior cortical connections of RRMS patients compared to controls. In contrast, longer-range thalamic connections were weakened. Furthermore, DMN thalamic connectivity universally decreased with reductions in cognitive processing speed measured by SDMT.

PLS brain scores identified an increase in whole-brain connectivity for RR compared to SP and HC subjects. Higher brain scores in RR subjects are indicative of network-specific increases in FC which could represent a compensatory response to neurodegeneration in MS. Cognitive scores generally showed little association with whole-brain rs-fMRI FC changes. Lastly, a plurality of affected connections resided in the DMN and ECN of subjects, suggesting possible RSN interactions and further investigation into potential mechanisms such as mixed rewiring effects.

This thesis highlights a systematic set of measures that can be used to map 7 T rsFMRI activation changes in MS. In particular, we see that RRMS subjects undergo FC adaptations in multiple RSN's, and at multiple spatial scales. The results advance and supplement a with

a growing body of literature that combines structural imaging measures of tissue with measures of local and overall brain activation.

7. References

1. Eric Widmaier; Hershel Raff; Kevin Strang. *Vander's Human Physiology*. Vol 44.; 2011. doi:10.1088/1751-8113/44/8/085201
2. Baecher-Allan C, Kaskow BJ, Weiner HL. Multiple Sclerosis: Mechanisms and Immunotherapy. *Neuron*. 2018;97(4):742-768. doi:10.1016/j.neuron.2018.01.021
3. Atkins GJ, Amor S, Fletcher JM, Mills KHG. *The Biology of Multiple Sclerosis*. Cambridge: Cambridge University Press; 2009. doi:10.1017/CBO9780511979088
4. Cerqueira JJ, Compston DAS, Geraldes R, et al. Time matters in multiple sclerosis: Can early treatment and long-term follow-up ensure everyone benefits from the latest advances in multiple sclerosis? *J Neurol Neurosurg Psychiatry*. 2018;89(8):844-850. doi:10.1136/jnnp-2017-317509
5. Lim SY, Constantinescu CS. Current and future disease-modifying therapies in multiple sclerosis. *Int J Clin Pract*. 2010;64(5):637-650. doi:10.1111/j.1742-1241.2009.02261.x
6. Saidha S, Eckstein C, Calabresi PA. New and emerging disease modifying therapies for multiple sclerosis. *Ann N Y Acad Sci*. 2012;1247(1):117-137. doi:10.1111/j.1749-6632.2011.06272.x
7. Ceccarelli A, Bakshi R, Neema M. MRI in multiple sclerosis: A review of the current literature. *Curr Opin Neurol*. 2012;25(4):402-409. doi:10.1097/WCO.0b013e328354f63f
8. Stankiewicz JM, Neema M, Ceccarelli A. Iron and multiple sclerosis. *Neurobiol Aging*. 2014;35(SUPPL.2):S51-S58. doi:10.1016/j.neurobiolaging.2014.03.039
9. Greicius MD, Supekar K, Menon V, Dougherty RF. Resting-state functional connectivity reflects structural connectivity in the default mode network. *Cereb Cortex*. 2009;19(1):72-78. doi:10.1093/cercor/bhn059
10. Honey CJ, Sporns O, Cammoun L, et al. Predicting human resting-state functional connectivity from structural connectivity. *Proc Natl Acad Sci U S A*. 2009;106(6):2035-2040. doi:10.1073/pnas.0811168106
11. Betzel RF, Byrge L, He Y, Goñi J, Zuo XN, Sporns O. Changes in structural and functional connectivity among resting-state networks across the human lifespan.

Neuroimage. 2014;102(P2):345-357. doi:10.1016/j.neuroimage.2014.07.067

12. Zhang HY, Wang SJ, Liu B, et al. Resting brain connectivity: Changes during the progress of Alzheimer disease. *Radiology*. 2010;256(2):598-606. doi:10.1148/radiol.10091701
13. Manning KY, Schranz A, Bartha R, et al. Multiparametric MRI changes persist beyond recovery in concussed adolescent hockey players. *Neurology*. 2017;89(21):2157-2166. doi:10.1212/WNL.0000000000004669
14. Brown RW, Cheng Y-CN, Haacke M, Thompson MR, Venkatesan R. *Magnetic Resonance Imaging: Physical Principles and Sequence Design, 2nd Edition*. Vol 15.; 2014.
15. McRobbie DW, Moore EA, Graves MJ, Prince MR. *MRI From Picture to Proton*. 2nd Editio. Cambridge University Press; 2007. https://mcgill.on.worldcat.org/oclc/982452338.
16. Chavhan GB, Babyn PS, Thomas B, Shroff MM, Haacke EM. Principles, Techniques, and Applications of T2*-based MR Imaging and Its Special Applications. *RadioGraphics*. 2009;29(5):1433-1449. doi:10.1148/rg.295095034
17. Ladd ME, Bachert P, Meyerspeer M, et al. Pros and cons of ultra-high-field MRI/MRS for human application. *Prog Nucl Magn Reson Spectrosc*. 2018;109:1-50. doi:10.1016/j.pnmrs.2018.06.001
18. Food and Drug Administration. Guidance for Industry and Food and Drug Administration Staff - Criteria for Significant Risk Investigations of Magnetic Resonance Diagnostic Devices. *Silver Spring, MD FDA;*. 2008. http://www.fda.gov/RegulatoryInformation/Guidances/ucm072686.htm.
19. Schepkin VD, Grant SC, Cross TA. In vivo MR Imaging at 21.1 T. 14(4):2-5. http://www.magnet.fsu.edu/mediacenter/factsheets/documents/invivomri-maglabreports-2007-v14-i4.pdf.
20. Polimeni JR, Fischl B, Greve DN, Wald LL. Laminar analysis of 7T BOLD using an imposed spatial activation pattern in human V1. *Neuroimage*. 2010;52(4):1334-1346. doi:10.1016/j.neuroimage.2010.05.005
21. Tian P, Teng IC, May LD, et al. Cortical depth-specific microvascular dilation underlies laminar differences in blood oxygenation level-dependent functional MRI signal. *Proc*

Natl Acad Sci U S A. 2010;107(34):15246-15251. doi:10.1073/pnas.1006735107

22. Hoult DI. The Principle of Reciprocity in Signal Strength Calculations. *Concepts Magn Reson*. 2000;12(4):173-187.
23. Barth M, Poser BA. Advances in high-field bold fmri. *Materials (Basel)*. 2011;4(11):1941-1955. doi:10.3390/ma4111941
24. Duyn JH, Van Gelderen P, Li TQ, De Zwart JA, Koretsky AP, Fukunaga M. High-field MRI of brain cortical substructure based on signal phase. *Proc Natl Acad Sci U S A*. 2007;104(28):11796-11801. doi:10.1073/pnas.0610821104
25. Duyn JH. The future of ultra-high field MRI and fMRI for study of the human brain. *Neuroimage*. 2012;62(2):1241-1248. doi:10.1016/j.neuroimage.2011.10.065
26. Gati JS, Menon RS, Uğurbil K, Rutt BK. Experimental determination of the BOLD field strength dependence in vessels and tissue. *Magn Reson Med*. 1997;38(2):296-302. doi:10.1002/mrm.1910380220
27. Fox PT, Raichle ME. Focal physiological uncoupling of cerebral blood flow and oxidative metabolism during somatosensory stimulation in human subjects. *Proc Natl Acad Sci U S A*. 1986;83(4):1140-1144. doi:10.1073/pnas.83.4.1140
28. Worden M, Schneider W. Cognitive Task Design for FMRl Timecourse of Hemodynamic Response for Two Areas of Activation. *Int J*. 1995;6:253-270.
29. Li M, Newton AT, Anderson AW, Ding Z, Gore JC. Characterization of the hemodynamic response function in white matter tracts for event-related fMRI. *Nat Commun*. 2019;10(1):1-11. doi:10.1038/s41467-019-09076-2
30. Biswal B, Yetkin FZ, Haughton VM, Hyde JS. Functional connectivity in the motor cortex of resting human brain using echo-planar MRI. *Magn Reson Med*. 1995;34(4):537-541. doi:10.1002/mrm.1910340409
31. Raichle ME, MacLeod AM, Snyder AZ, Powers WJ, Gusnard DA, Shulman GL. A default mode of brain function. *Proc Natl Acad Sci U S A*. 2001;98(2):676-682. doi:10.1073/pnas.98.2.676
32. Raichle ME. The Brain's Default Mode Network. *Annu Rev Neurosci*. 2015;38(1):433-447. doi:10.1146/annurev-neuro-071013-014030
33. De Luca M, Beckmann CF, De Stefano N, Matthews PM, Smith SM. fMRI resting state networks define distinct modes of long-distance interactions in the human brain.

Neuroimage. 2006;29(4):1359-1367. doi:10.1016/j.neuroimage.2005.08.035

34. Hafkemeijer A, Altmann-Schneider I, Oleksik AM, et al. Increased functional connectivity and brain atrophy in elderly with subjective memory complaints. *Brain Connect*. 2013;3(4):353-362. doi:10.1089/brain.2013.0144
35. Gardini S, Venneri A, Sambataro F, et al. Increased Functional Connectivity in the Default Mode Network in Mild Cognitive Impairment: A Maladaptive Compensatory Mechanism Associated with Poor Semantic Memory Performance. *J Alzheimer's Dis*. 2015;45(2):457-470. doi:10.3233/JAD-142547
36. Ferreira LK, Regina ACB, Kovacevic N, et al. Aging effects on whole-brain functional connectivity in adults free of cognitive and psychiatric disorders. *Cereb Cortex*. 2016;26(9):3851-3865. doi:10.1093/cercor/bhv190
37. Veer IM, Beckmann CF, van Tol MJ, et al. Whole brain resting-state analysis reveals decreased functional connectivity in major depression. *Front Syst Neurosci*. 2010;4(September):1-10. doi:10.3389/fnsys.2010.00041
38. Tahedl M, Levine SM, Greenlee MW, Weissert R, Schwarzbach J V. Functional connectivity in multiple sclerosis: Recent findings and future directions. *Front Neurol*. 2018;9(OCT):1-18. doi:10.3389/fneur.2018.00828
39. Kurtzke JF. Geography in multiple sclerosis. *J Neurol*. 1977;215 n1.
40. Simpson S, Mina S, Morris H, Mahendran S, Taylor B, Boggild M. The epidemiology of multiple sclerosis in the Isle of Man: 2006-2011. *Acta Neurol Scand*. 2015;132(6):381-388. doi:10.1111/ane.12405
41. Khalid R. Contributing factors in multiple sclerosis and the female sex bias. *Immunol Lett*. 2014;162(1):223-232. doi:10.1016/j.imlet.2014.09.004
42. Tienari P, Bonetti A, Pihlaja H, Saastamoinen KP, Rantamäki T. Multiple sclerosis in G: Genes and geography. *Clin Neurol Neurosurg*. 2006;108(3):223-226. doi:10.1016/j.clineuro.2005.11.004
43. Kurtzke JF. Rating neurologic impairment in multiple sclerosis: An expanded disability status scale (EDSS). *Neurology*. 1983;33(11):1444-1452. doi:10.1212/wnl.33.11.1444
44. Atkins G, Amor S, Fletcher J, Mills K. *The Biology of Multiple Sclerosis*. Cambridge: Cambridge University Press; 2012. doi:10.1017/CBO9780511979088

45. Charil A, Zijdenbos AP, Taylor J, et al. Statistical mapping analysis of lesion location and neurological disability in multiple sclerosis: Application to 452 patient data sets. *Neuroimage*. 2003;19(3):532-544. doi:10.1016/S1053-8119(03)00117-4
46. Barkhof F. The clinico-radiological paradox in multiple sclerosis revisited. *Curr Opin Neurol*. 2002;15(3):239-245. doi:10.1097/00019052-200206000-00003
47. Cohen JA, Cutter GR, Fischer JS, et al. Use of the multiple sclerosis functional composite as an outcome measure in a phase 3 clinical trial. *Arch Neurol*. 2001;58(6):961-967. doi:10.1001/archneur.58.6.961
48. Al-Temaimi R, AbuBaker J, Al-khairi I, Alroughani R. Remyelination modulators in multiple sclerosis patients. *Exp Mol Pathol*. 2017;103(3):237-241. doi:10.1016/j.yexmp.2017.11.004
49. Hanafy KA, Sloane JA. Regulation of remyelination in multiple sclerosis. *FEBS Lett*. 2011;585(23):3821-3828. doi:10.1016/j.febslet.2011.03.048
50. Bramow S, Frischer JM, Lassmann H, et al. Demyelination versus remyelination in progressive multiple sclerosis. *Brain*. 2010;133(10):2983-2998. doi:10.1093/brain/awq250
51. Vercellino M, Plano F, Votta B, Mutani R, Giordana MT, Cavalla P. Grey Matter Pathology in Multiple Sclerosis. *J Neuropathol Exp Neurol*. 2005;64(12):1101-1107. doi:10.1097/01.jnen.0000190067.20935.42
52. Kutzelnigg A, Lassmann H. Cortical lesions and brain atrophy in MS. *J Neurol Sci*. 2005;233(1-2):55-59. doi:10.1016/j.jns.2005.03.027
53. Gilmore CP, Bö L, Owens T, Lowe J, Esiri MM, Evangelou N. Spinal cord gray matter demyelination in multiple sclerosis - A novel pattern of residual plaque morphology. *Brain Pathol*. 2006;16(3):202-208. doi:10.1111/j.1750-3639.2006.00018.x
54. Fisher E, Lee JC, Nakamura K, Rudick RA. Gray matter atrophy in multiple sclerosis: A longitudinal study. *Ann Neurol*. 2008;64(3):255-265. doi:10.1002/ana.21436
55. Fisniku LK, Chard DT, Jackson JS, et al. Gray matter atrophy is related to long-term disability in multiple sclerosis. *Ann Neurol*. 2008;64(3):247-254. doi:10.1002/ana.21423
56. Rombouts SARB, Lazeron RHC, Scheltens P, et al. Visual activation patterns in patients with optic neuritis: An f MRI pilot study. *Neurology*. 1998;50(6):1896-1899.

doi:10.1212/WNL.50.6.1896

57. Werring DJ, Brex PA, Moseley IF, et al. Recovery from optic neuritis is associated with a change in the distribution of cerebral response to visual stimulation: A functional magnetic resonance imaging study. *J Neurol Neurosurg Psychiatry*. 2000;68(4):441-449. doi:10.1136/jnnp.68.4.441
58. Staffen W, Mair A, Zauner H, et al. Cognitive function and fMRI in patients with multiple sclerosis: Evidence for compensatory cortical activation during an attention task. *Brain*. 2002;125(6):1275-1282. doi:10.1093/brain/awf125
59. Parry AMM, Scott RB, Palace J, Smith S, Matthews PM. Potentially adaptive functional changes in cognitive processing for patients with multiple sclerosis and their acute modulation by rivastigmine. *Brain*. 2003;126(12):2750-2760. doi:10.1093/brain/awg284
60. Scarpina F, Tagini S. The stroop color and word test. *Front Psychol*. 2017;8(APR):1-8. doi:10.3389/fpsyg.2017.00557
61. Filippi M, Rocca MA, Colombo B, et al. Functional magnetic resonance imaging correlates of fatigue in multiple sclerosis. *Neuroimage*. 2002;15(3):559-567. doi:10.1006/nimg.2001.1011
62. Ciccarelli O, Toosy AT, Marsden JF, et al. Functional response to active and passive ankle movements with clinical correlations in patients with primary progressive multiple sclerosis. *J Neurol*. 2006;253(7):882-891. doi:10.1007/s00415-006-0125-z
63. Raichle ME, Snyder AZ. A default mode of brain function: A brief history of an evolving idea. *Neuroimage*. 2007;37(4):1083-1090. doi:10.1016/j.neuroimage.2007.02.041
64. Rocca MA, Valsasina P, Absinta M, et al. Default-mode network dysfunction and cognitive impairment in progressive MS. *Neurology*. 2010;74(16):1252-1259. doi:10.1212/WNL.0b013e3181d9ed91
65. Bonavita S, Gallo A, Sacco R, et al. Distributed changes in default-mode resting-state connectivity in multiple sclerosis. *Mult Scler J*. 2011;17(4):411-422. doi:10.1177/1352458510394609
66. Roosendaal SD, Schoonheim MM, Hulst HE, et al. Resting state networks change in clinically isolated syndrome. *Brain*. 2010;133(6):1612-1621.

doi:10.1093/brain/awq058

67. Liu Y, Dai Z, Duan Y, et al. Whole brain functional connectivity in clinically isolated syndrome without conventional brain MRI lesions. *Eur Radiol*. 2016;26(9):2982-2991. doi:10.1007/s00330-015-4147-8
68. Sbardella E, Tona F, Petsas N, et al. Functional connectivity changes and their relationship with clinical disability and white matter integrity in patients with relapsing–remitting multiple sclerosis. *Mult Scler J*. 2015;21(13):1681-1692. doi:10.1177/1352458514568826
69. Rocca MA, Pravatà E, Valsasina P, et al. Hippocampal-DMN disconnectivity in MS is related to WM lesions and depression. *Hum Brain Mapp*. 2015;36(12):5051-5063. doi:10.1002/hbm.22992
70. Gabilondo I, Rilo O, Ojeda N, et al. The influence of posterior visual pathway damage on visual information processing speed in multiple sclerosis. *Mult Scler J*. 2017;23(9):1276-1288. doi:10.1177/1352458516676642
71. Cruz Gómez ÁJ, Ventura Campos N, Belenguer A, Ávila C, Forn C. Regional Brain Atrophy and Functional Connectivity Changes Related to Fatigue in Multiple Sclerosis. He Y, ed. *PLoS One*. 2013;8(10):e77914. doi:10.1371/journal.pone.0077914
72. Rocca MA, Valsasina P, Fazio R, et al. Brain connectivity abnormalities extend beyond the sensorimotor network in peripheral neuropathy. *Hum Brain Mapp*. 2014;35(2):513-526. doi:10.1002/hbm.22198
73. Schoonheim MM, Geurts JJG, Wiebenga OT, et al. Changes in functional network centrality underlie cognitive dysfunction and physical disability in multiple sclerosis. *Mult Scler J*. 2014;20(8):1058-1065. doi:10.1177/1352458513516892
74. Filippi M, Rocca MA, Falini A, et al. Correlations between structural CNS damage and functional MRI changes in primary progressive MS. *Neuroimage*. 2002;15(3):537-546. doi:10.1006/nimg.2001.1023
75. Pantano P, Mainero C, Lenzi D, et al. A longitudinal fMRI study on motor activity in patients with multiple sclerosis. *Brain*. 2005;128(9):2146-2153. doi:10.1093/brain/awh549
76. Leonard G, Milner B, Jones L. Performance on unimanual and bimanual tapping tasks

by patients with lesions of the frontal or temporal lobe. *Neuropsychologia*. 1988;26(1):79-91. doi:10.1016/0028-3932(88)90032-2

77. Benedict RHB, Deluca J, Phillips G, LaRocca N, Hudson LD, Rudick R. Validity of the Symbol Digit Modalities Test as a cognition performance outcome measure for multiple sclerosis. *Mult Scler*. 2017;23(5):721-733. doi:10.1177/1352458517690821
78. Wechsler D. *WAIS-III: Wechsler Adult Intelligence Scale--Third Edition Administration and Scoring Manual*. San Antonio, TX: Psychological Corporation; 1997.
79. Beck A, Steer R, Brown. *The Beck Depression Inventory - Second Edition Manual*. San Antonio, TX: The Psychological Corporation; 1996.
80. Fisk JD, Ritvo PG, Ross L, Haase DA, Marrie TJ, Schlech WF. Measuring the functional impact of fatigue: Initial validation of the fatigue impact scale. *Clin Infect Dis*. 1994;18:S79-S83. doi:10.1093/clinids/18.Supplement_1.S79
81. Neuropsychology T. Specific Impairments of Planning Author (s): T . Shallice Source : Philosophical Transactions of the Royal Society of London . Series B , Biological Published by : Royal Society Stable URL : http://www.jstor.com/stable/2395870 REFERENCES Linked referenc. 1982;298(1089):199-209.
82. Fischer A.J.; Kniker, J.E.; Rudick, R.A.; Cutter, G. JS. J. Multiple Sclerosis Functional Composite (MSFC): Administration and scoring manual. Revised, October 2001. *Natl Mult Scler Soc*. 2001:6-9.
83. Fischl B, Dale AM. Measuring the thickness of the human cerebral cortex. *Neuroimage*. 1999;9(6 PART II).
84. Fischl B, Rajendran N, Busa E, et al. Cortical folding patterns and predicting cytoarchitecture. *Cereb Cortex*. 2008;18(8):1973-1980. doi:10.1093/cercor/bhm225
85. Fischl B, Van Der Kouwe A, Destrieux C, et al. Automatically Parcellating the Human Cerebral Cortex. *Cereb Cortex*. 2004;14(1):11-22. doi:10.1093/cercor/bhg087
86. Fischl B, Dale AM. Measuring the thickness of the human cerebral cortex from magnetic resonance images. *Proc Natl Acad Sci U S A*. 2000;97(20):11050-11055. doi:10.1073/pnas.200033797
87. Smith SM. Fast robust automated brain extraction. *Hum Brain Mapp*. 2002;17(3):143-155. doi:10.1002/hbm.10062

88. Smith SM, Jenkinson M, Woolrich MW, et al. Advances in functional and structural MR image analysis and implementation as FSL. *Neuroimage*. 2004;23(SUPPL. 1):208-219. doi:10.1016/j.neuroimage.2004.07.051
89. Fonov V, Evans AC, Botteron K, Almli CR, McKinstry RC, Collins DL. Unbiased average age-appropriate atlases for pediatric studies. *Neuroimage*. 2011;54(1):313-327. doi:10.1016/j.neuroimage.2010.07.033
90. Zhang Y, Brady M, Smith S. Segmentation of brain MR images through a hidden Markov random field model and the expectation-maximization algorithm. *IEEE Trans Med Imaging*. 2001;20(1):45-57. doi:10.1109/42.906424
91. Greve DN, Fischl B. Accurate and robust brain image alignment using boundary-based registration. *Neuroimage*. 2009;48(1):63-72. doi:10.1016/j.neuroimage.2009.06.060
92. Jenkinson M, Bannister P, Brady M, Smith S. Improved Optimization for the Robust and Accurate Linear Registration and Motion Correction of Brain Images. *Neuroimage*. 2002;17(2):825-841. doi:10.1006/nimg.2002.1132
93. Jenkinson M, Smith S. A global optimisation method for robust affine registration of brain images. *Med Image Anal*. 2001;5(2):143-156. doi:10.1016/S1361-8415(01)00036-6
94. Avants BB, Tustison NJ, Wu J, Cook PA, Gee JC. ANTS: Advanced Open-Source Tools for Normalization And Neuroanatomy. *Neuroinformatics*. 2011;9(4):381-400. doi:10.1007/s12021-011-9109-y
95. Tustison NJ, Avants BB. Explicit B-spline regularization in diffeomorphic image registration. *Front Neuroinform*. 2013;7(DEC):1-13. doi:10.3389/fninf.2013.00039
96. Beckmann CF, Smith SM. Probabilistic Independent Component Analysis for Functional Magnetic Resonance Imaging. *IEEE Trans Med Imaging*. 2004;23(2):137-152. doi:10.1109/TMI.2003.822821
97. Caballero-Gaudes C, Reynolds RC. Methods for cleaning the BOLD fMRI signal. *Neuroimage*. 2017;154(December 2016):128-149. doi:10.1016/j.neuroimage.2016.12.018
98. Jenkinson M. Measuring Transformation Error by RMS Deviation. *FMRIB Tech Rep*. 1999;TR99(MJ1):1-4. doi:10.1017/CBO9781107415324.004

99. Woolrich MW, Ripley BD, Brady M, Smith SM. Temporal autocorrelation in univariate linear modeling of FMRI data. *Neuroimage*. 2001;14(6):1370-1386. doi:10.1006/nimg.2001.0931
100. Sladky R, Friston KJ, Tröstl J, Cunnington R, Moser E, Windischberger C. Slice-timing effects and their correction in functional MRI. *Neuroimage*. 2011;58(2):588-594. doi:10.1016/j.neuroimage.2011.06.078
101. Griffanti L, Douaud G, Bijsterbosch J, et al. Hand classification of fMRI ICA noise components. *Neuroimage*. 2017;154(June 2016):188-205. doi:10.1016/j.neuroimage.2016.12.036
102. Smith AM, Lewis BK, Ruttimann UE, et al. Investigation of low frequency drift in fMRI signal. *Neuroimage*. 1999;9(5):526-533. doi:10.1006/nimg.1999.0435
103. Skudlarski P, Constable RT, Gore JC. ROC analysis of statistical methods used in functional MRI: Individual subjects. *Neuroimage*. 1999;9(3):311-329. doi:10.1006/nimg.1999.0402
104. Yuen NH, Osachoff N, Chen JJ. Intrinsic Frequencies of the Resting-State fMRI Signal: The Frequency Dependence of Functional Connectivity and the Effect of Mode Mixing. *Front Neurosci*. 2019;13(September):1-17. doi:10.3389/fnins.2019.00900
105. Beckmann CF, Jenkinson M, Woolrich MW, et al. Applying FSL to the FIAC data: Model-based and model-free analysis of voice and sentence repetition priming. *Hum Brain Mapp*. 2006;27(5):380-391. doi:10.1002/hbm.20246
106. Chai XJ, Castañán AN, Öngür D, Whitfield-Gabrieli S. Anticorrelations in resting state networks without global signal regression. *Neuroimage*. 2012. doi:10.1016/j.neuroimage.2011.08.048
107. Kelly REJ, Alexopoulos GS, Wang Z, et al. Visual inspection of independent components: Defining a procedure for artifact removal from fMRI data. *J Neurosci Methods*. 2010;189(2):233-245. doi:10.1016/j.jneumeth.2010.03.028.Visual
108. Nickerson LD, Smith SM, Öngür D, Beckmann CF. Using dual regression to investigate network shape and amplitude in functional connectivity analyses. *Front Neurosci*. 2017;11(MAR):1-18. doi:10.3389/fnins.2017.00115
109. Shirer WR, Ryali S, Rykhlevskaia E, Menon V, Greicius MD. Decoding subject-driven cognitive states with whole-brain connectivity patterns. *Cereb Cortex*.

2012;22(1):158-165. doi:10.1093/cercor/bhr099

110. Whitfield-Gabrieli S, Nieto-Castanon A. Conn: A Functional Connectivity Toolbox for Correlated and Anticorrelated Brain Networks. *Brain Connect*. 2012;2(3):125-141. doi:10.1089/brain.2012.0073
111. McIntosh AR, Mišić B. Multivariate Statistical Analyses for Neuroimaging Data. *Annu Rev Psychol*. 2013;64(1):499-525. doi:10.1146/annurev-psych-113011-143804
112. Smith SM, Fox PT, Miller KL, et al. Correspondence of the brain's functional architecture during activation and rest. *Proc Natl Acad Sci U S A*. 2009;106(31):13040-13045. doi:10.1073/pnas.0905267106
113. Schöpf V, Windischberger C, Kasess CH, Lanzenberger R, Moser E. Group ICA of resting-state data: A comparison. *Magn Reson Mater Physics, Biol Med*. 2010;23(5-6):317-325. doi:10.1007/s10334-010-0212-0
114. Zalesky A, Fornito A, Bullmore ET. Network-based statistic: Identifying differences in brain networks. *Neuroimage*. 2010;53(4):1197-1207. doi:10.1016/j.neuroimage.2010.06.041
115. McIntosh AR, Mišić B. Multivariate Statistical Analyses for Neuroimaging Data. *Ssrn*. 2013. doi:10.1146/annurev-psych-113011-143804
116. Griffanti L, Douaud G, Bijsterbosch J, et al. Hand classification of fMRI ICA noise components. *Neuroimage*. 2017;154(December 2016):188-205. doi:10.1016/j.neuroimage.2016.12.036
117. Nassi JJ, Callaway EM. Parallel processing strategies of the primate visual system. *Nat Rev Neurosci*. 2009;10(5):360-372. doi:10.1038/nrn2619
118. Poldrack RA, Nichols T, Mumford J. *Handbook of Functional MRI Data Analysis*.; 2011. doi:10.1017/cbo9780511895029
119. Faivre A, Rico A, Zaaraoui W, et al. Assessing brain connectivity at rest is clinically relevant in early multiple sclerosis. *Mult Scler J*. 2012;18(9):1251-1258. doi:10.1177/1352458511435930
120. Petsas N, Tinelli E, Lenzi D, et al. Evidence of Impaired Brain Activity Balance after Passive Sensorimotor Stimulation in Multiple Sclerosis. *PLoS One*. 2013;8(6):1-10. doi:10.1371/journal.pone.0065315
121. Petsas N, Tomassini V, Filippini N, et al. Impaired Functional Connectivity Unmasked

by Simple Repetitive Motor Task in Early Relapsing-Remitting Multiple Sclerosis. *Neurorehabil Neural Repair*. 2015;29(6):557-565. doi:10.1177/1545968314558600

122. Audoin B, Davies GR, Finisku L, Chard DT, Thompson AJ, Miller DH. Localization of grey matter atrophy in early RRMS: A longitudinal study. *J Neurol*. 2006;253(11):1495-1501. doi:10.1007/s00415-006-0264-2
123. Minagar A, Barnett MH, Benedict RHB, et al. The thalamus and multiple sclerosis: Modern views on pathologic, imaging, and clinical aspects. *Neurology*. 2013;80(2):210-219. doi:10.1212/WNL.0b013e31827b910b
124. Pfefferbaum A, Chanraud S, Pitel AL, et al. Cerebral blood flow in posterior cortical nodes of the default mode network decreases with task engagement but remains higher than in most brain regions. *Cereb Cortex*. 2011;21(1):233-244. doi:10.1093/cercor/bhq090
125. Liu Y, Liang P, Duan Y, et al. Altered thalamic functional connectivity in multiple sclerosis. *Eur J Radiol*. 2015;84(4):703-708. doi:10.1016/j.ejrad.2015.01.001
126. Tona F, Petsas N, Sbardella E, et al. Multiple sclerosis: Altered thalamic resting-state functional connectivity and its effect on cognitive function. *Radiology*. 2014;271(3):814-821. doi:10.1148/radiol.14131688
127. Shen K kai, Welton T, Lyon M, et al. Structural core of the executive control network: A high angular resolution diffusion MRI study. *Hum Brain Mapp*. 2020;41(5):1226-1236. doi:10.1002/hbm.24870
128. Rocca MA, Valsasina P, Martinelli V, et al. Large-scale neuronal network dysfunction in relapsing-remitting multiple sclerosis. *Neurology*. 2012;79(14):1449-1457. doi:10.1212/WNL.0b013e31826d5f10
129. Littow H, Huossa V, Karjalainen S, et al. Aberrant functional connectivity in the default mode and central executive networks in subjects with schizophrenia - a whole-brain resting-state ICA study. *Front Psychiatry*. 2015;6(FEB):1-10. doi:10.3389/fpsyt.2015.00026
130. Rudko DA, Solovey I, Gati JS, Kremenchutzky M, Menon RS. Multiple sclerosis: Improved identification of disease-relevant changes in gray and white matter by using susceptibility-based MR imaging. *Radiology*. 2014;272(3):851-864. doi:10.1148/radiol.14132475

131. Salimi-Khorshidi G, Douaud G, Beckmann CF, Glasser MF, Griffanti L, Smith SM. Automatic denoising of functional MRI data: Combining independent component analysis and hierarchical fusion of classifiers. *Neuroimage*. 2014;90(0):449-468. doi:10.1016/j.neuroimage.2013.11.046
132. Pruim RHR, Mennes M, van Rooij D, Llera A, Buitelaar JK, Beckmann CF. ICA-AROMA: A robust ICA-based strategy for removing motion artifacts from fMRI data. *Neuroimage*. 2015;112:267-277. doi:10.1016/j.neuroimage.2015.02.064
133. Mišic B, Betzel RF, De Reus MA, et al. Network-level structure-function relationships in human neocortex. *Cereb Cortex*. 2016;26(7):3285-3296. doi:10.1093/cercor/bhw089
134. Smith A. *Symbol Digits Modalities Test: Manual*. Los Angeles: Western Psychological Services; 2007.

Appendix

Table A.1: *Subject Demographic Data*

Cohort		Age (Years)	Education (Years)		Sex
Healthy Controls	Mean	43.56	16.13	Male	6
	S.E.	4.94	0.62	Female	9
				Total	**15**
Relapsing Remitting MS	Mean	43.45	15.00	Male	5
	S.E.	5.22	0.51	Female	9
				Total	**14**
Secondary Progressive MS	Mean	49.80	13.82	Male	3
	S.E.	1.53	0.48	Female	8
				Total	**11**

Note: Age and education measured at time of scan. S.E. = standard error.

Table A.2: *Disease Duration and Expanded Disability Status Scale Scores of Multiple Sclerosis Cohorts*

Cohort		Disease Duration (Months)	EDSS
Relapsing Remitting MS	Mean	133.62	1.90
	S.E.	111.18	0.33
Secondary Progressive MS	Mean	221.64	4.60
	S.E.	28.35	0.51

Note: Disease duration and EDSS measured at time of scan. S.E. = standard error

Table A.3: *Neuropsychological Test Results*

Cohort		LTT (Mean Correct)		SDMT	WAIS-III	MFIS	BDI-II	TOL-2	PASAT-2	PASAT-3
		(In Phase)	(Out of Phase)	(Z-Score)	(Percentile)	(Raw Score /84)	(Raw Score /40)	(Scaled Average /100)	(Z-Score)	(Z-Score)
Healthy Controls	Mean	77.133	37.833	0.415	82.200	22.533	5.933	96.743	0.082	0.006
	S.E.	4.929	2.607	0.200	4.173	3.241	1.248	1.626	0.184	0.230
Relapsing Remitting MS	Mean	62.929	31.643	-0.228	60.786	33.000	9.857	100.000	-0.228	-0.341
	S.E.	6.422	3.628	0.249	7.892	5.297	2.507	1.898	0.264	0.276
Secondary Progressive MS	Mean	49.227	23.455	-0.777	36.545	46.273	12.182	92.883	-1.402	-1.121
	S.E.	5.871	2.748	0.351	9.976	2.770	1.892	2.906	0.575	0.438

Note: All scores were measured at the time of the scan. S.E = standard error. LTT = Leonard Tapping Test[76]. SDMT = Symbol Digit Modalities Test[134]. WAIS-III = Wechsler Adult Intelligence Scale Test, Edition III[78]. MFIS = Modified Fatigue Impact Scale[80]. BDI-II = Beck Depression Inventory Edition II[79]. TOL-2 = Tower of London 2nd Edition[81]. PASAT = Paced Auditory Serial Addition Test[82].